

# An advanced approach for the generation of complex cellular material representative volume elements using distance fields and level sets

B. Sonon<sup>1</sup> · B. François<sup>1</sup> · T. J. Massart<sup>1</sup>

Received: 31 August 2014 / Accepted: 7 May 2015 / Published online: 14 June 2015  
© Springer-Verlag Berlin Heidelberg 2015

**Abstract** A general and widely tunable method for the generation of representative volume elements for cellular materials based on distance and level set functions is presented. The approach is based on random tessellations constructed from random inclusion packings. A general methodology to obtain arbitrary-shaped tessellations to produce disordered foams is presented and illustrated. These tessellations can degenerate either in classical Voronoï tessellations potentially additively weighted depending on properties of the initial inclusion packing used, or in Laguerre tessellations through a simple modification of the formulation. A versatile approach to control the particular morphology of the obtained foam is introduced. Specific local features such as concave triangular Plateau borders and non-constant thickness heterogeneous coatings can be built from the tessellation in a straightforward way and are tuned by a small set of parameters with a clear morphological interpretation.

**Keywords** Cellular materials · Microstructure generation · Representative volume element · Level sets · Open-cell foams · Closed-cell foams

## 1 Introduction

Cellular materials are characterized by a morphology based on a space-filling assembly of near-polyhedral volumes (cells) separated by walls. An archetype for this kind of materials is the equilibrated liquid foam, for which cells originate from bubbles that are separated by tensioned liquid films,

those meeting 3-by-3 at 120°, and forming so-called Plateau borders [1,2]. However, solid foams such as closed-cell metallic foams obtained by directly foaming a liquid metal (e.g. Al), polymer (e.g. PU) open-cell foams, or open-cell metal foams obtained either by coating an existing polymer foam or by casting liquid metal in a polymer foam-based mould also present morphologies strongly similar to liquid foams, more or less close to the Plateau equilibrium. Grain assembly in polycrystalline metals or rocks can also be seen as derived from a cellular medium structure, more or less compliant with Plateau conditions. More complex biomaterials such as trabecular bones, wood or tissues characterized by a well-grown extra cellular matrix also share several morphological similarities with cellular materials, and were already idealized as such in mechanical models by some authors [3,4].

The physical behavior (e.g. mechanical, acoustical, thermal, transport-related, . . .) of this type of materials strongly depends on their microstructure and this particular link is the subject of an increasing number of studies, for various fields of application, mechanics and acoustics being the most represented. Next to purely experimental studies [5–11], computational models at the microstructural scale, or homogenization-based and multi-scale models may bring a more in-depth understanding of the relationship between the local morphological features of the material and its global behavior. Closely related to experimental characterization are the numerical simulations that use the real geometry of materials, thanks to the use of computer-aided tomography data, to build finite element models [12–15]. In spite of the valuable results they provide (in particular when coupled with real tests on scanned samples), such studies however present the same kind of drawbacks as in purely experimental studies, i.e. the cost and time for sample preparation, scanning and data post-processing may constrain authors to study limited

✉ T. J. Massart  
thmassar@ulb.ac.be

<sup>1</sup> BATir, Building, Architecture & Town Planning, Université Libre de Bruxelles (ULB), CP 194/2, Brussels, Belgium

numbers of samples. Therefore, general conclusions which ideally should require broader parametric studies are difficult to reach. Another class of models that may bring valuable insight on this aspect makes use of idealized microstructure geometry descriptions to explore and understand elementary mechanisms related with the particular morphology of the material [16–32]. In spite of the fact that such models cannot fully resemble scanned data, they provide the opportunity to single out the influence of specific morphological parameters of the material for various physical phenomena.

The success of the latter approach is however strongly constrained by the ability of the geometrical model to represent as realistically as possible the morphological features of the material in a more or less parametrized way. The identification of such idealized representative volume elements (RVEs) remains an important and debated question for cellular materials in general.

To this end, deterministic models have been derived from the observation of liquid foams. One of the first of such models is the Kelvin model [33] which consists of a regular packing of (slightly curved) tetra(kai)decahedra (truncated octahedra). This model was (more than 100 years later) improved by the Weaire–Phelan model [34] made of two different types of cells, dodecahedra and tetradecehedra. Such regular models however fail to represent foams with non-uniform bubble sizes or more disordered, out-of-equilibrium solid foams. It was shown in [35] that morphological features of those models such as the number of faces by cell and edges by cell face significantly diverge from real foams, which lead to another 11-faced polyhedral model to be proposed. Next to those polyhedral cell models, some simple geometries based on regular bars or plates assemblies were also used [18, 21, 29]. Within such models, plate thickness or lattice node positions can be randomized to account for the natural variability of the material. Packings of overlapping spheres were also used for this purpose, randomized [25] or not [19].

More realistic and versatile representations were introduced by the use of random tessellations, i.e. Voronoï tessellations on random point distributions [16, 24] and Laguerre tessellations on random sphere packings to obtain multi-sized cell arrangements [30, 36]. It should be mentioned that similar microstructural models are used for polycrystalline materials [37–49], demonstrating a degree of similitude of the morphology of these materials with foam-based media. The morphological properties of Laguerre-based models have been well characterized, compared and fitted to real foams [50, 51], supporting with quantitative arguments that solid foam are not in Plateau equilibrium [52]. These generation methods represent very well the size distribution of cells and some other morphological parameters (face-by-cell count, edge-by-face count, dihedral and interior angles, ...) but produces very regular geometries, i.e. cell walls and/or

struts are straight. Other morphological features such as wall/strut thickness and strut sections are not determined by the tessellation itself and need to be constructed afterwards. The available examples cited above keep those aspects simple, i.e. with constant thickness wall/strut and circular strut sections.

The real shape of struts arising from Plateau borders geometry in open-cell polymer foams or polymer-based metal foams usually presents typical triangular concave sections of variable size and concavity, as reported by micrograph inspections [9, 53]. Metal-coated polymer foams present moreover hollow struts due to the elimination of the polymer preform, also well visible on micrographs [10] or reconstructed 3D data [13]. Some intermediate states between closed and open foams may exist (i.e. partially reticulated), with highly variable pore throat sizes, resulting in highly variable strut sizes and shapes [6, 54]. The throat size or the closed face rate in partially reticulated PU foams have been reported to have an important effect on the acoustic behavior of such foams either experimentally [7] or with the help of numerical simulations [28, 32]. These latter numerical studies used a Kelvin unit cell as geometrical model, with variable thickness cylindrical struts and planar membrane with circular holes. To the best of our knowledge, only one publication describes and tests a generalizable and automated way to generate the exact shape of Plateau borders [22]. Their approach consists in applying a surface minimization process on a base tessellation with the software Surface Evolver. The methodology was illustrated with a single Weaire–Phelan unit cell, which does not allow assessing how Surface Evolver performs on more complex base tessellations. This methodology seems focused on foams very close to the equilibrium, and is presumably difficult to use for more disordered solid foam morphologies.

In this paper, we present and illustrate a general and widely tunable methodology for the generation of RVEs for cellular materials making use of distance and level set functions. The approach is, like most others, based on random tessellations constructed from random inclusion packings. However, we present here a general procedure to obtain arbitrary-shaped tessellations enabling to produce disordered foam microstructures, more representative of metallic and out-of-equilibrium foams. These arbitrary-shaped tessellations can degenerate in classical Voronoï tessellations, potentially additively weighted, depending on properties of the initial inclusion packing used. Starting from the RVE generation procedure defined in [55] in a 2D setting, the present contribution develops additional tools to extend the approach for cellular materials in a 3D context. We furthermore introduce a versatile approach to control the particular morphology of the obtained foam. This is achieved by defining a “Plateau” level set function, by setting up a procedure allowing the extraction of geometries from multiple level set functions for the proper reproduction of sharp edges, and by incorpo-

rating additional features such as concave triangular Plateau borders and non-constant thickness heterogeneous coatings are built from the tessellation in a straightforward way and tuned by a small set of parameters with a clear morphological interpretation. Finally, it is emphasized that the generation process can be constrained to produce periodic RVEs without heavy modification of the implementation.

The paper is organized as follow. We first introduce and define some concepts and notations that will be used in subsequent developments (Sect. 2). In particular, specific distance functions are introduced and the concept of level set function is defined. We then present the basis of our approach to generate RVEs for open and closed foams (Sect. 3). It includes a short explanation of the method to produce arbitrary-shaped tessellations as well as illustrations of its use to generate closed foam RVEs (Sect. 3.1). It is followed by the introduction of a specific level set function used to generate open foam RVEs (Sect. 3.2) as well as the explanation on how to extract properly the resulting geometry (Sect. 3.3). We continue then with advanced strategies to obtain more subtle aspects of the morphologies for the generated foams (Sect. 4). We cover techniques to finely tune the shape of generated Plateau borders (Sect. 4.1), to introduce spatial variation on controlling parameters (Sect. 4.2) and to add a coating phase on the generated foams, potentially non-uniform and/or multi-layered (Sect. 4.3). We finally shortly present some quantitative morphological parameters characterizing the obtained foams (Sect. 5). The paper is closed by a discussion section (Sect. 6) and conclusions (Sect. 7).

## 2 Notations and definitions

In the sequel,  $\Omega_{RVE}$  denotes the 3D domain of an RVE. In this paper, we use cubic domains exclusively (square for 2D illustrations) and all dimensions are given with respect to this cube side length.

In 3D, *level sets* are surfaces defined implicitly by relationships of the type  $f(\mathbf{x}) = k$ , in which  $\mathbf{x}$  represents spatial coordinates, the functions  $f(\mathbf{x})$  are generally called *level set functions*. Such surfaces are closed (except on boundaries of the definition domain of  $f(\mathbf{x})$ ), non-self-intersecting, non-branched (manifold only) and orientable. In particular, they are everywhere perpendicular to the gradient of  $f(\mathbf{x})$  and their curvatures are reflected by the local values of the second spatial derivatives of  $f(\mathbf{x})$ .

Level set functions and all other functions in this paper will be evaluated through a discrete set of data sampled on regular 3D grids of  $n^3$  points. The level set geometries are obtained by contouring these discrete function representations, as done for computed tomography data reconstruction, by a classical contouring method (e.g. the marching cube [56,57], the dual contouring [58,59]).

$\Phi_i$  denotes a closed surface representing the boundary of an inclusion  $i$ , member of a set  $\mathbf{I}$  gathering all inclusions of a packing (represented by white dashed line on Fig. 1a).

$\Omega_i^-$  is the domain inside  $\Phi_i$ ,  $\Omega_i^+$  is the domain outside  $\Phi_i$  (see Fig. 1b, the negative domain is grey-shaded).

$DS_i(\mathbf{x})$  is the signed distance field of  $\Phi_i$ . This 3D function is negative on  $\Omega_i^-$  and positive on  $\Omega_i^+$  and is a natural level set function for the inclusion  $i$  which is represented implicitly by the 0 level set of it. The order of continuity of a signed distance field is inherited from  $\Phi_i$  everywhere except on the medial axis of the interface where it is  $C^0$ . The medial axis of  $\Phi_i$  is defined as the locus of points where the center of a sphere can be placed such that the sphere exactly touches  $\Phi_i$  at least on two points, without intersecting it [60].

$DN_k(\mathbf{x})$  is the  $k$ -th neighbor distance field. It gives at every position  $\mathbf{x}$  the distance from the  $k$ -th nearest  $\Phi_i$  in the packing  $\mathbf{I}$ . These functions for  $k$  equal 1,2 and 3 are illustrated in Fig. 1b, c and d.  $DN_1(\mathbf{x})$  can be used as a level set function representing all inclusions in the packing. It is emphasized that those functions were already introduced and used in the context of heterogeneous material microstructure generation in our previous work [55], and were denoted “ $LS_k$ ” in that paper.

$NN_k(\mathbf{x})$  is the  $k$ -th neighbor identity map. It is an integer discontinuous function equal for each  $\mathbf{x}$  to the index of the  $k$ -th nearest inclusion from  $\mathbf{x}$  in the set  $\mathbf{I}$  (see Fig. 1a for  $NN_1$ , where distinct values of the function are represented by distinct colors). These functions are by-products of the  $DN_k$  functions evaluation.

$\mathbf{J}_k(\mathbf{x})$  is the set  $\mathbf{I}$  without all  $NN_m(\mathbf{x})$  with  $m$  in  $[1:k - 1]$  (and  $\mathbf{J}_1(\mathbf{x}) = \mathbf{I}$  for every  $\mathbf{x}$ ).

$DN_1(\mathbf{x})$  can be computed as:

$$DN_1(\mathbf{x}) = \min_i(DS_i(\mathbf{x})), \quad i \in \mathbf{I}. \tag{1}$$

Other  $DN_k(\mathbf{x})$  can be computed as:

$$DN_k(\mathbf{x}) = \min_j(DS_j(\mathbf{x})), \quad j \in \mathbf{J}_k(\mathbf{x}). \tag{2}$$

${}^I\Theta_i$  is the domain where the inclusion  $i$  is the first nearest inclusion, i.e. where  $NN_1(\mathbf{x}) = i$ , or the set of points  $\mathbf{x}$  closer to inclusion  $i$  than to any other (red area on Fig. 1a).

${}^O\Theta_i$  is the domain where  $NN_1(\mathbf{x}) \neq i$  (non-red area on Fig. 1a). The preceding superscript O and I stand for “outer” and “inner”.

$\Phi_{\Theta_i}$  is the boundary of  ${}^I\Theta_i$  (white plain line on Fig. 1a).

$\Phi_{\Theta}$  is the union of all  $\Phi_{\Theta_i}$  (black and white plain lines on Fig. 1a).

The general notation  ${}^I f_i(\mathbf{x})$  and  ${}^O f_i(\mathbf{x})$  refers to two functions associated with domains  ${}^I\Theta_i$  and  ${}^O\Theta_i$ .

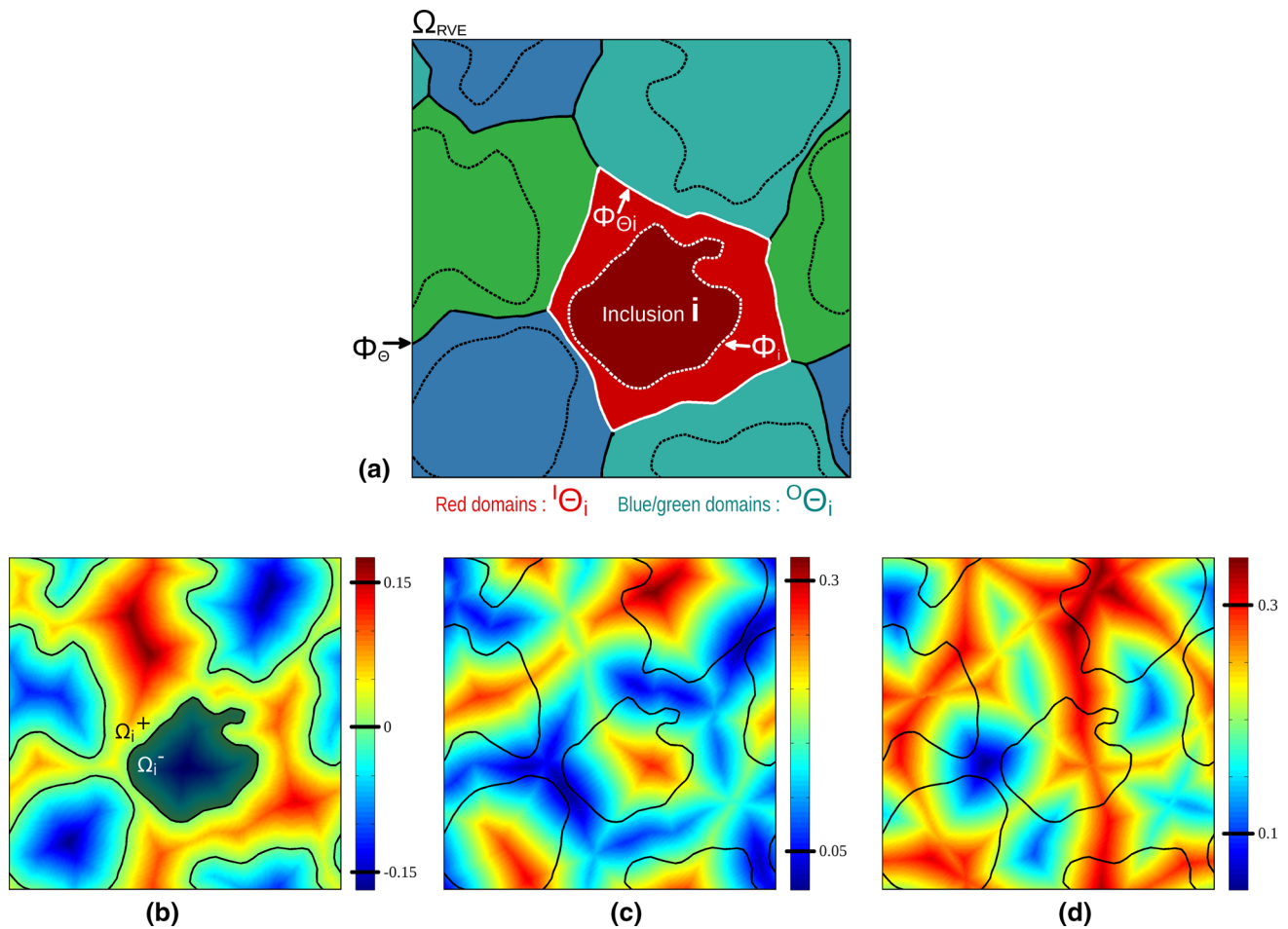


**Fig. 1** Definition and notations illustrated for a 2D simple inclusion packing. **a** Domains and loci. *Dashed lines* denote the inclusion boundaries, while *plain lines* stand for  $\Phi_\Theta$ . **b** Function  $DN_1$ , **c** function  $DN_2$

and **d** function  $DN_3$ . Distance are given relative to the RVE size, *black lines* are inclusion boundaries  $\Phi_i$ . (Color figure online)

### 3 General cellular morphologies generation

#### 3.1 Building an arbitrary-shaped tessellation: the “Voronoi” level set function

We previously explained how to build an arbitrary-shaped tessellation with the help of neighboring distance fields of an inclusion packing in a former work [55]. For the sake of clarity and completeness we reintroduce here the basic ideas that were presented and illustrated for the case of polycrystalline material RVEs generation.

From an arbitrary-shaped inclusion packing, we can define a tessellation made by the assembly of all domains  $I\Theta_i$  that enclose, for each inclusion  $i$ , points closer to this inclusion than to others. This tessellation degenerates in additively weighted Voronoi and classical Voronoi tessellations for multi-sized sphere packings and points distributions (or mono-sized sphere packings), respectively. The first and second neighbor distance fields of the initial inclusion packing can be combined to construct implicitly this tessellation. We

define the “Voronoi” level set function as

$$O_V(\mathbf{x}) = DN_2(\mathbf{x}) - DN_1(\mathbf{x}). \tag{3}$$

This function is exactly zero at loci equidistant from the two nearest inclusions, i.e. on faces of the tessellation, and positive elsewhere. It is illustrated for 2D packings in Fig. 2. It is emphasized that as the inclusion signed distance fields used are negative inside their inclusions, the initial packing can present inter-penetrated inclusions without affecting the quality of the result. Actually, a variant of this function was specifically used in [61] to handle spurious overlapping of yarns in the generation of woven composite RVEs.

Laguerre tessellations can also be produced this way, using multi-sized spheres as initial packings and replacing the signed Euclidean distance function  $DS_i$  by a sphere power distance when evaluating functions  $DN_k$ . Laguerre tessellations are appreciated because they produce easily multi-sized cell tessellations while keeping plane cell faces and straight face edges. In our opinion, the latter aspect is only a conve-

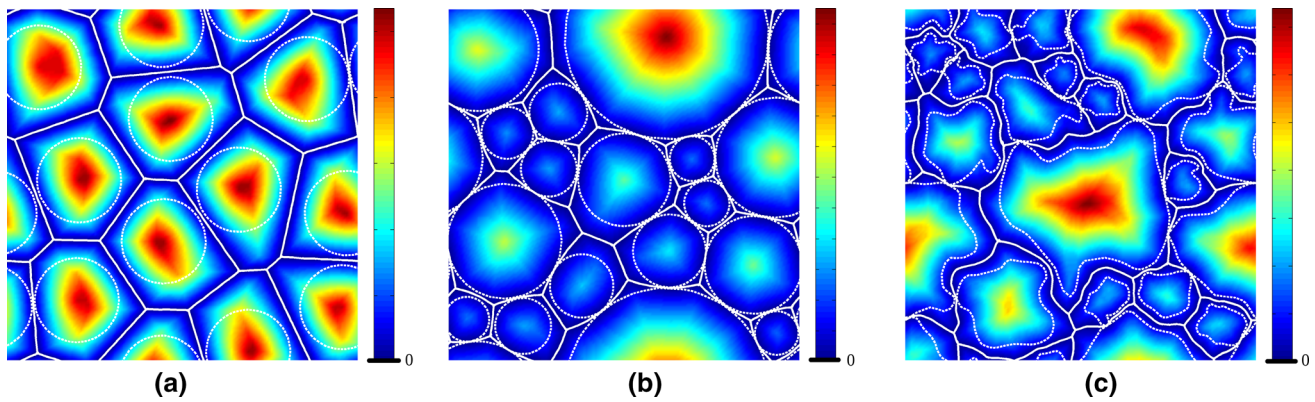


**Fig. 2** “Voronoi” level set functions. **a** For a mono-sized disk packing. **b** For a multi-sized disk packing. **c** For an arbitrary-shaped inclusion packing. *Dashed lines* are the inclusion boundaries  $\Phi_i$ , *plain lines* are the boundaries of the tessellation cells  $\Phi_{\Theta_i}$

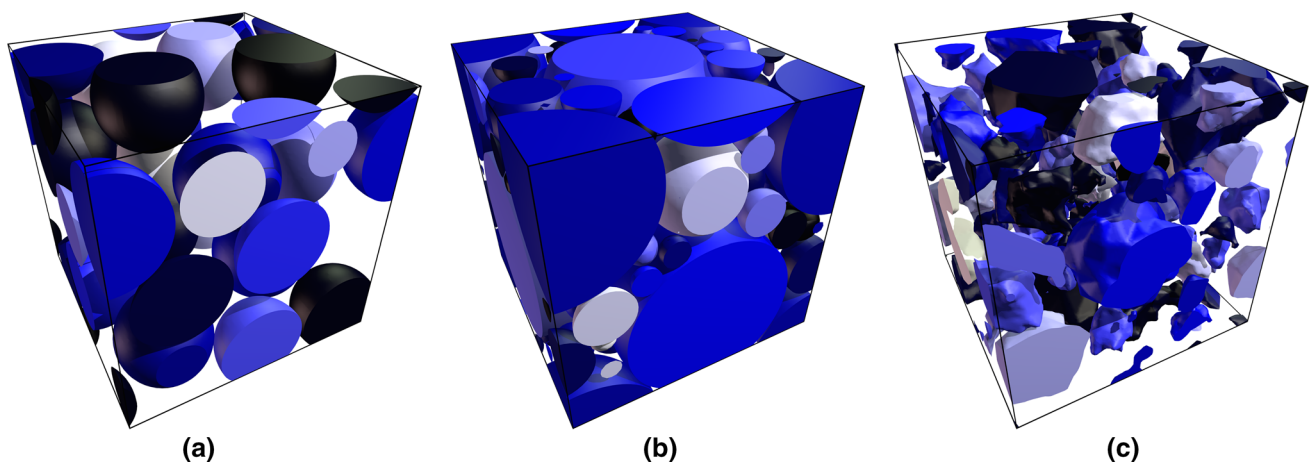


**Fig. 3** Initial packings used for illustrations. **a** Mono-sized sphere packing. **b** Multi-sized sphere packing. **c** Arbitrary-shaped inclusion packing

nient simplification, but is not motivated by the morphology of real foams. Actually, liquid foams with multi-sized bubbles exhibit larger pressures in small bubbles (causing foam coarsening with time by gas diffusion through liquid films). This causes films between bubbles to be slightly curved, rendering large bubbles concave. The additively weighted Voronoi tessellation generated by (3) on a multi-sized sphere packing seems better suited to generate this kind of feature (see Figs. 2b, 4b).

The function  $O_V$  alone can be used to extract a quasi-constant thickness closed cell geometry through level sets extracted from

$$O_V(\mathbf{x}) - t = 0. \tag{4}$$

We illustrate the use of this function on the basis of three base packings, obtained respectively from mono-sized spheres, multi-sized spheres and arbitrary-shaped inclusions, which are illustrated in Fig. 3. The RVEs obtained from such packings with  $t = 0.01$  are shown in Fig. 4.

In fact the local thickness of the extracted walls depends slightly on the relative angle of normals at nearest points of the first and second nearest inclusions on that local spot. In general this leads to thinner wall centers, and presents exactly a thickness  $t$  where the previously mentioned normals share the same orientation (and opposite directions). This effect increases with the wall mean thickness. A variant of  $O_V(\mathbf{x})$  introducing a weighting factor  $w$  associated with  $DN_2(\mathbf{x})$  may be used to build all intermediary situations between a completely space-filling tessellation ( $w = 1$ ) and the initial inclusion packing ( $w = 0$ ):

$$O'_V(\mathbf{x}) = w \cdot DN_2(\mathbf{x}) - DN_1(\mathbf{x}). \tag{5}$$

In order to obtain the original inclusion surface with  $w = 0$ , the parameter  $t$  in Eq. (4) should also be multiplied by  $w$ . An example using this alternative  $O'_V$  is given in Fig. 5, in which the packing from Fig. 3.c is used with  $t = 0.01$  and  $w = \{0.25|0.5|0.75\}$ . Such intermediary morphologies can be used to represent some porous mate-

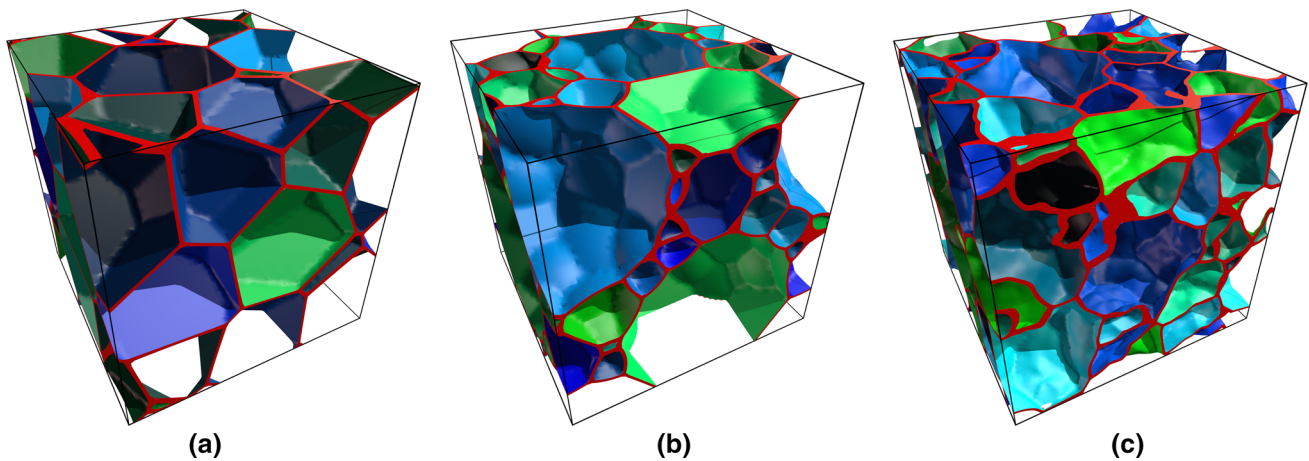


**Fig. 4** Closed cell RVE examples, generated from packings of Fig. 3 with  $t = 0.01$ . **a** From mono-sized sphere packing. **b** From multi-sized sphere packing. **c** From arbitrary-shaped inclusion packing

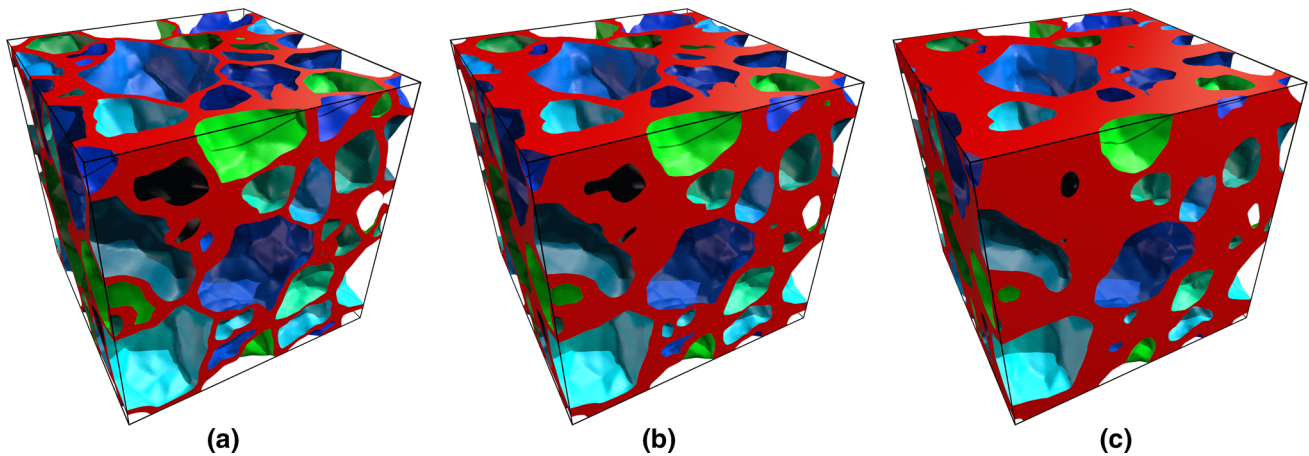


**Fig. 5** Intermediate RVEs between the closed cell foam ( $w = 1$ ) and the original inclusion packing ( $w = 0$ ). The RVE of Fig. 3.c is used with  $t = 0.01$ . **a**  $w = 0.75$ , **b**  $w = 0.5$ , **c**  $w = 0.25$ . The value  $w = 1$  gives

the RVE of Fig. 4c and  $w = 0$  would give back the original packing, with an offset of magnitude  $t$  on inclusions

materials that are not manufactured by foaming processes, for which the microstructure share more morphological features with inclusion-based morphologies. Metal foams obtained by liquid casting together with solid place holders (removed afterward, or hollow spheres) are examples of such type of porous media [62–64].

Extracting the zero level set of  $O_V$  is problematic because it is a minimum of the function that won't be properly extracted by a contouring algorithm. A modified “local” version of  $O_V$  is introduced further (Sect. 3.3) and can be used for the proper extraction of this particular level set.

### 3.2 Building open foam morphology: the “Plateau border” level set function

To produce open foam microstructures, a way should be defined to extract the edges of tessellation cells by the mean

of an ad-hoc level set function, giving them triangular sections. Combined with the knowledge that Plateau borders in liquid foams form at the intersection of three films, this suggests to combine the three first neighbor distance functions  $DN_1(\mathbf{x})$ ,  $DN_2(\mathbf{x})$  and  $DN_3(\mathbf{x})$  to build a relevant level set function. The following function, denoted  $O_P$  and called the “Plateau” level set function in the sequel, is exactly zero at locus where the distance from the three nearest inclusions is the same, and is positive elsewhere:

$$O_P(\mathbf{x}) = (DN_3(\mathbf{x}) + DN_2(\mathbf{x}))/2 - DN_1(\mathbf{x}). \quad (6)$$

This function is illustrated in 2D in Fig. 6. It is clear from this representation that the level set of this function consists of triangles with vertex lying on the tessellation cell boundaries extracted from  $O_V(\mathbf{x})$  (i.e.  $\Phi_\Theta$ ). In 3D, these level sets will generate triangular prisms centered on edges of the tessella-

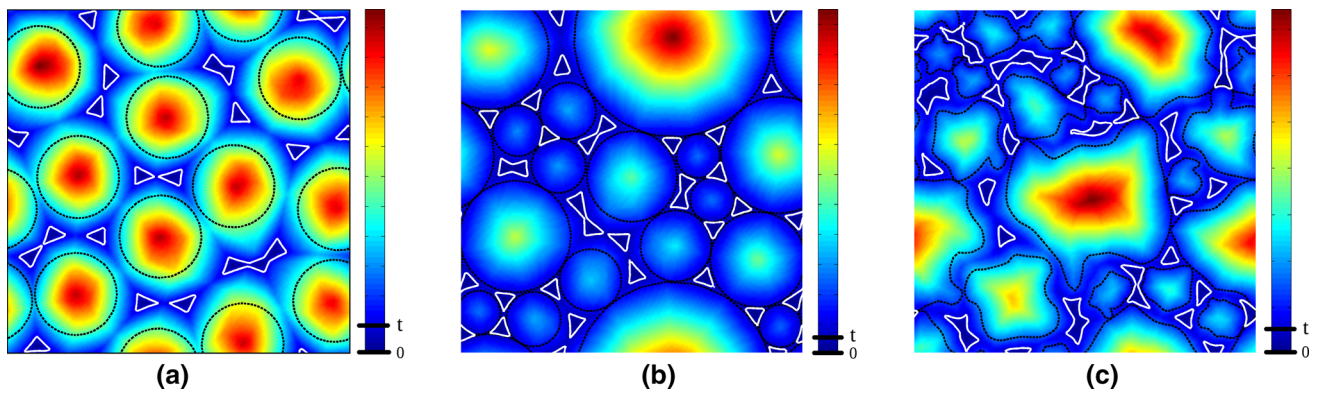


**Fig. 6** “Plateau” level set function, the level set  $t$  is drawn in with, *black dashed lines* are the initial inclusion boundaries. **a** For a mono-sized disk packing, **b** For a multi-sized disk packing, **c** For an arbitrary-shaped inclusion packing. (Color figure online)

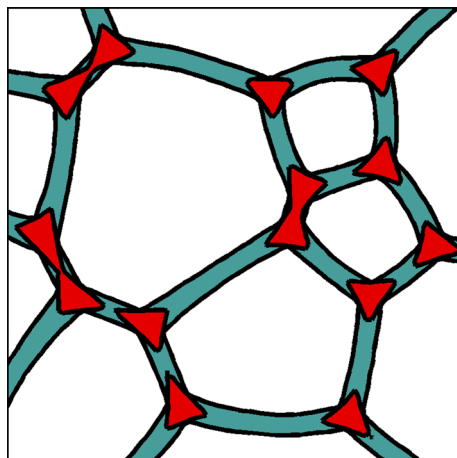


**Fig. 7** 2D illustration of the relation between cell wall extracted with (4) (*blue*) and Plateau border extracted with (7) (*red*) using the same value for  $t$ . The figure is a detail of the RVE used in Figs. 2b and 6b. (Color figure online)

tion, with lines generated by the triangle vertices of the prism section lying on  $\Phi_\Theta$ . This furnishes a natural way to build a Plateau-border-like geometry through

$$O_P(\mathbf{x}) - t = 0. \tag{7}$$

The parameter  $t$  can here be used to control the thickness of extracted borders. It is related to the parameter used in (4) such that the Plateau borders produced are the largest ones that could be completely contained in closed cell walls, as illustrated in Fig. 7.

Some typical resulting geometries obtained using this level set function are illustrated in Fig. 8. It is worth to remark that if the starting inclusion distribution is a made of mono-sized sphere, the Plateau borders extracted from  $O_P(\mathbf{x})$  are straight while for multi-sized spheres, they become slightly curved. For arbitrary-shaped inclusions, the extracted borders still present the same triangular section but are not straight

and present complex director curves. One can also remark that resulting Plateau borders are not concave, this aspect will be further elaborated in Sect. 6.

### 3.3 Sharp edges preservation: extracting geometry from multiple level set functions

The Plateau borders geometry presents sharp edges due to their triangular prism shape. Such sharp edges originate from a steep discontinuity of  $DN_k$  derivatives on  $\Phi_\Theta$ . Discrete level set functions are not well suited to handle such kinds of discontinuities for several reasons. It is indeed well-known that contouring algorithms fail to extract such sharp edges [65] (see Fig. 9a). Furthermore, several quantities computed using numerical derivatives of  $O_V$  or  $O_P$ , such as normal and curvature fields [66] will also be imprecise and/or locally wrong near  $\Phi_\Theta$ .

To overcome these difficulties, the global geometry can be split into an assembly of smooth surfaces, extracted from separate level set functions, their common curves being the problematic sharp edges (see Fig. 9b). The three “faces” of each Plateau border are determined from the three nearest inclusions at this place. This aspect is emphasized on Figs. 8, 9b and similar figures, in which the surfaces “coming from” each inclusions are rendered with distinct colors. Therefore, by constructing an individual level set function for each inclusion one can extract separately the three “faces” of each Plateau border and avoid the problem of sharp edges. However, for open cells, such surfaces are not closed but present holes in the cell faces. As the contouring of a level set function always produces closed surfaces, an additional slicing operation is required to obtain these holes. A second individual level set function for each inclusion is then required and is used to slice the surface formerly obtained by contouring the first level set function. The slicing of a 3D triangulated surface according to a level set function is very similar to the contouring of a 2D level set function. The values of the

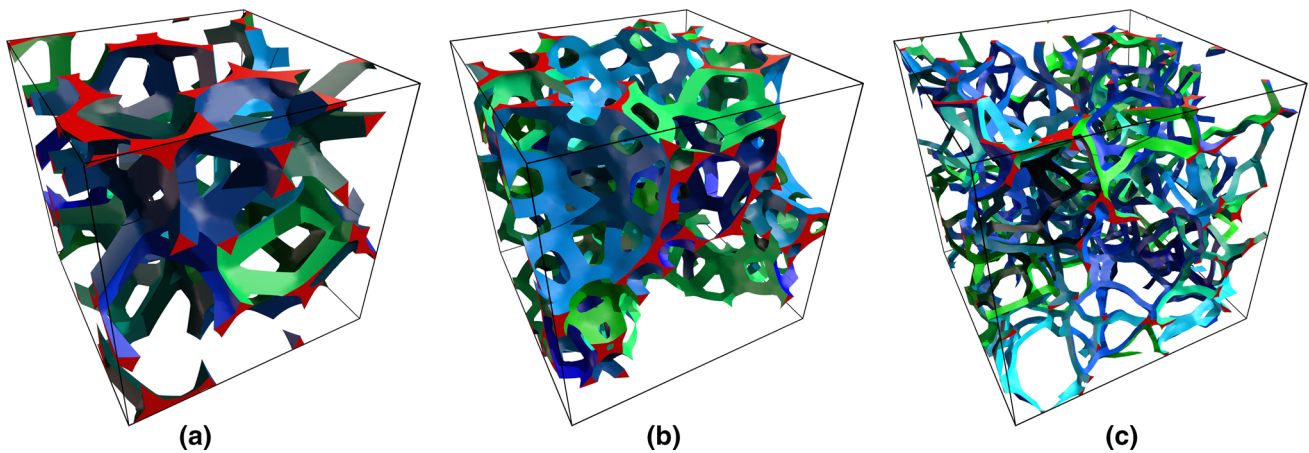


**Fig. 8** Open cell RVE examples, generated from packing of Fig. 3. **a** From mono-sized sphere,  $t = 0.04$ . **b** From multi-sized spheres,  $t = 0.02$ . **c** From arbitrary-shaped inclusions,  $t = 0.01$

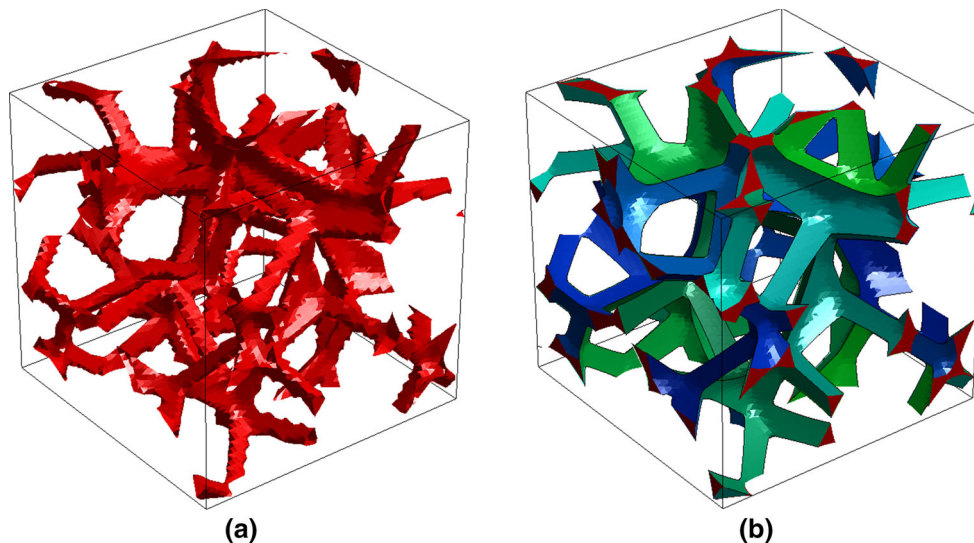


**Fig. 9** Sharp edge issue illustration. **a** Result of a single level set function extraction. **b** Result of a multi level set function extraction. Problematic sharp edges are highlighted with *black lines*. (Color figure online)

second level set function are interpolated on vertices of the surface extracted from the first, and a “marching triangle” algorithm is then applied to this triangulated surface to perform the slicing. This approach is illustrated in Fig. 10 for an isolated cell.

The two “local” level set functions for each inclusion are built without modification of the  $O_P$  definition, “global” functions  $DN_k$  are modified to construct two “local” functions for each inclusion denoted “inner” and “outer” neighboring distance function (and marked by a preceding superscript “I” and “O”),  ${}^I DN_{ki}$  and  ${}^O DN_{ki}$ . Functions  ${}^I O_{Pi}$  and  ${}^O O_{Pi}$  are then computed using the same relations (6) as for the “global” function. The “inner” local level set is used to extract the surface “coming from” the considered inclusion, while the “outer” local level set is used to slice it.

It is emphasized that the functions  ${}^I DN_{ki}$  and  ${}^O DN_{ki}$  have no geometrical meaning, they are rather ad-hoc functions constructed from  $DN_k$  under the following constraints :

(I) Inner functions should be equal to global functions inside  ${}^I \Theta_i$  and  $C^1$  continuous across  $\Phi_{\Theta_i}$ . Indeed, inside  ${}^I \Theta_i$ , an inner function is intended to yield the same level set surface as its global equivalent while its particular value on  ${}^O \Theta_i$  does not matter as the level set produced in this domain will not remain after the slicing. The only requirement consists of the surface to be smooth on  $\Phi_{\Theta_i}$  to properly extract it by contouring.

(II) Outer functions should be equal to global functions only on  $\Phi_{\Theta_i}$  and  $C^1$  continuous across  $\Phi_{\Theta_i}$ . An outer function is only required to slice properly the level set extracted from an inner function. As a consequence, its particular value is

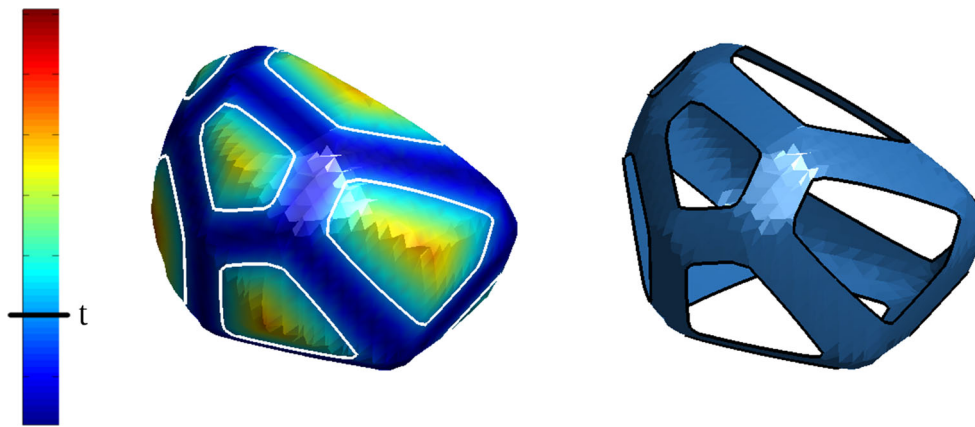


**Fig. 10** Multi level set approach illustrated on an isolated cell. **a** Surface resulting of the contouring of the “inner” level set function  ${}^1O_{P_i}(\mathbf{x})$ . The “outer” level set function  ${}^0O_{P_i}(\mathbf{x})$  is plotted on the surface. **b** Surface after the slicing by the “outer” level set function

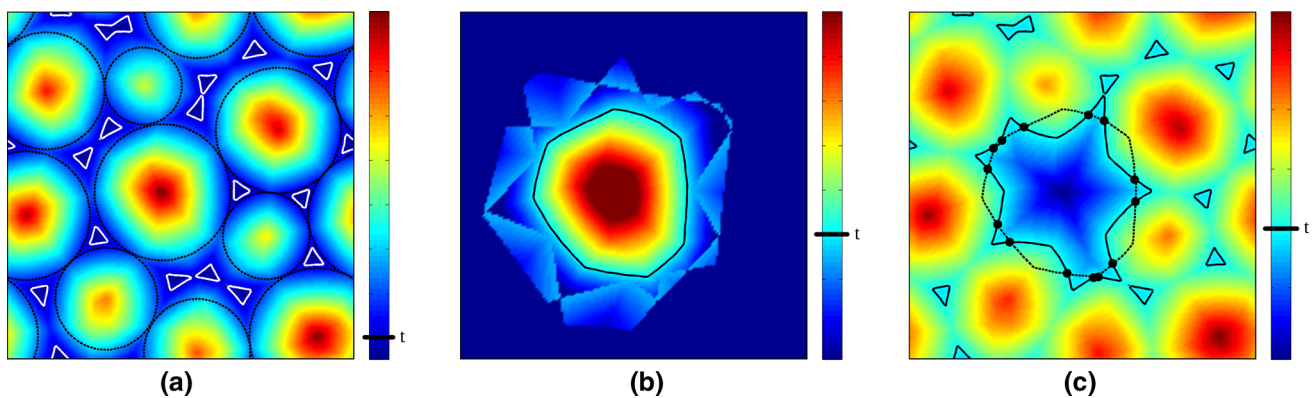


**Fig. 11** Global and local “Plateau” level set function. **a** Global function  $O_P(\mathbf{x})$ , the  $t$  level set is drawn in *white*, *dashed black lines* are initial inclusion boundaries. **b** Local function  ${}^1O_{P_i}(\mathbf{x})$  of the central inclusion, the  $t$  level set is drawn in *black*. **c** Local function  ${}^0O_{P_i}(\mathbf{x})$  of the central

inclusion, the  $t$  level set is drawn in *plain black*. The *dashed line* is the  $t$  level set of  ${}^1O_{P_i}(\mathbf{x})$  while *black dots* are the slice loci. (Color figure online)

not important, except on  $\Phi_{\Theta_i}$  where it should be equal to the corresponding global function.

These constrains are formulated according to the features needed for  ${}^1O_{P_i}$  and  ${}^0O_{P_i}$  without restriction on the way to achieve them. As  $DN_k$  are assemblies of patches coming from all  $DS_i$ , a simple reorganization of those patches is possible in order to fulfill the two preceding statements for  ${}^1DN_{ki}$  and  ${}^0DN_{ki}$ . As  $O_P$  is a simple linear combination of  $DN_k$ , these two statements will also be verified for  ${}^1O_{P_i}$  and  ${}^0O_{P_i}$ , as illustrated for a 2D packing in Fig. 11. A careful analysis of  $DN_1$ ,  $DN_2$  and  $DN_3$  permits to derive the following transformations:

$${}^1DN_{1i}(\mathbf{x}) = DS_i(\mathbf{x}), \tag{8a}$$

$${}^1DN_{2i}(\mathbf{x}) = DN_2(\mathbf{x}) \text{ where } NN_2(\mathbf{x}) \neq i, \tag{8b}$$

$${}^1DN_{2i}(\mathbf{x}) = DN_1(\mathbf{x}) \text{ where } NN_2(\mathbf{x}) = i, \tag{8c}$$

$${}^0DN_{1i}(\mathbf{x}) = DN_1(\mathbf{x}) \text{ where } NN_1(\mathbf{x}) \neq i, \tag{8d}$$

$${}^0DN_{1i}(\mathbf{x}) = DN_2(\mathbf{x}) \text{ where } NN_1(\mathbf{x}) = i, \tag{8e}$$

$${}^0DN_{2i}(\mathbf{x}) = DN_2(\mathbf{x}) \text{ where } NN_1(\mathbf{x}) \neq i, \tag{8f}$$

$${}^0DN_{2i}(\mathbf{x}) = DN_1(\mathbf{x}) \text{ where } NN_1(\mathbf{x}) = i, \tag{8g}$$

with  ${}^1DN_{3i}$  and  ${}^0DN_{3i}$  being both equal to  $DN_3$  because the latter is already  $C^1$  continuous across  $\Phi_{\Theta_i}$ . Those transformations are further detailed and illustrated in Appendix. One might remark that for an inclusion  $i$ , instead of building the “outer” function, the “inner” functions of all other inclusions can be used to slice the surface coming from inclusion  $i$ . However, this requires storing all “inner” functions for the complete domain in memory, which would quickly lead to overflow for large RVEs (large numbers of inclusions). Therefore, it is preferred to evaluate both “inner” and “outer” functions, that do not have to be kept in memory once the surface coming from inclusion  $i$  is extracted. It should be mentioned that quantities such as the derivatives of  $O_P$  can again be accurately computed using the relevant “inner” or “outer” level set functions. On  $\Phi_{\Theta_i}$  two values are available reflecting the fact that those derivatives are discontinuous on this particular locus and are only defined “left and right to this discontinuity”.

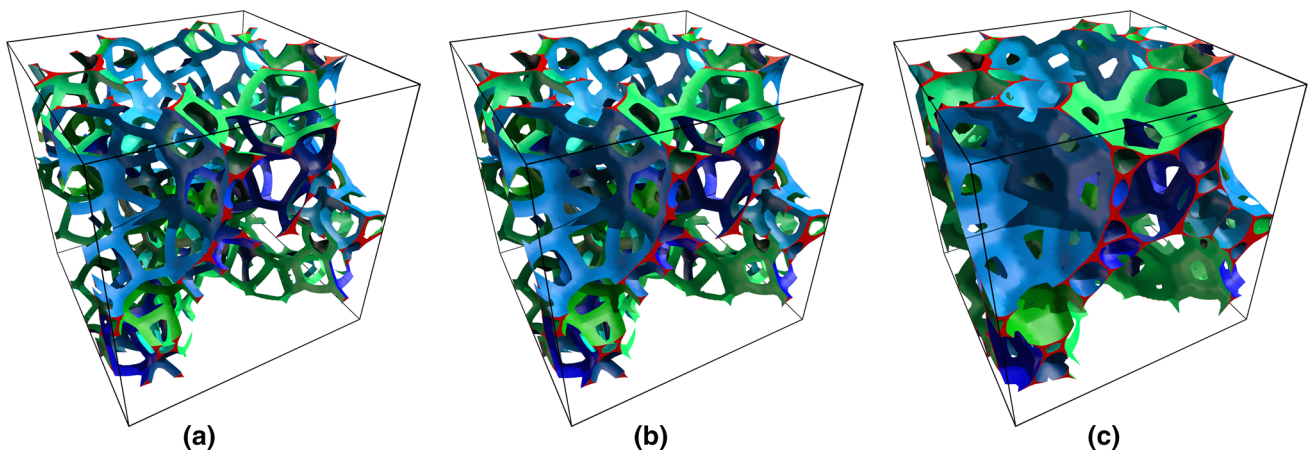


**Fig. 12** Open/closed intermediate situation using. **a**  $a = 0.25$ . **b**  $a = 0.5$ . **c**  $a = 0.75$

Useful values of these functions are limited to a narrow band enclosing the surface to extract. For large numbers of inclusions, a significant fraction of the computation time may be saved by limiting the computation domain to this band. The global function  $O_P$  and the neighbor identity maps  $NN_k$  can be used to localize a priori this domain of interest for each inclusion according to

$$DOI_i \equiv ((NN_1(\mathbf{x}) = i)|(NN_2(\mathbf{x}) = i)|(NN_3(\mathbf{x}) = i)) \& ((O_V(\mathbf{x}) - t > -e) \& (O_V(\mathbf{x}) - t < e)) \quad (9)$$

with  $e$  being the half thickness of the band, that should be at least 2 times the discretization size (set by the grid of points on which functions are evaluated).

We finally emphasize that building a finite element mesh for the generated RVEs is not trivial (even though not impossible). This problem will be discussed in Sect. 6.

## 4 Generation of advanced morphological features

### 4.1 Plateau border morphology

Generally, plateau border sections are not triangular prisms but unions of three concave surfaces. Other materials may present an intermediate morphology between open and closed foams. Some techniques may be used to tune more precisely the resulting Plateau borders morphology. We first show how to combine  $O_V$  and  $O_P$  to obtain intermediate situations between fully open and closed foams. A simple way to control the concavity curvature of the Plateau borders is then outlined. We finally indicate how to combine cases with differing parameters to produce a larger range of variations.

#### *Open/closed intermediates*

A natural way to achieve intermediate open/closed situations is to use both  $O_V$  and  $O_P$  in a linear combination, considering level sets defined by:

$$a \cdot O_V(\mathbf{x}) + (1 - a) \cdot O_P(\mathbf{x}) - t = 0, \quad (10)$$

with  $0 < a < 1$ , acting as an open/closed ratio. This approach indeed simply consists in a weighted averaging of the two geometries obtained with (4) and (7). Problems arising from sharp edges are simply treated as before, but the entire relation (10) has now to be written in “inner” and “outer” versions using “inner” and “outer” versions of both  $O_V$  and  $O_P$ . Figure 12 illustrates the use of this relation with 3 different values of the parameter  $a$ .

#### *Concavity*

To obtain concave Plateau borders starting from the presented methodology, a way to tweak the relation (7) to make it produce concave surfaces is introduced. Basically, subtracting a constant value to a level set function results in an outward displacement of the surface it defines. Similarly, subtracting a non-constant function induces local changes of the surface curvature. If this non-constant function is only  $C^0$  continuous, this will introduce infinite curvatures and create unwanted sharp edges. A  $C^1$  function prevents this behavior but may introduce curvature jumps, while the use of a  $C^2$  continuous function would ensure the curvature to vary smoothly. The idea is then to build a function, preferably  $C^2$ , that vanishes on Plateau border sharp edges and takes negative values near Plateau border surfaces, to “push” inward these surfaces without moving sharp edges. To this end, the following function is used:

$$O_K(\mathbf{x}) = \min(0, (((DN_3(\mathbf{x}) - DN_2(\mathbf{x}))/2)^2 - t^2)/2t). \quad (11)$$

This function is illustrated in 2D on Fig. 13b. To properly visualize this function, one should consider its value on a line passing by two sharp edges of a Plateau border and contained in a plane perpendicular to it (black/white lines on Fig. 13a/b). On this line, the operator  $DS_3(\mathbf{x}) - DS_2(\mathbf{x})$  varies from 0 to  $2t$

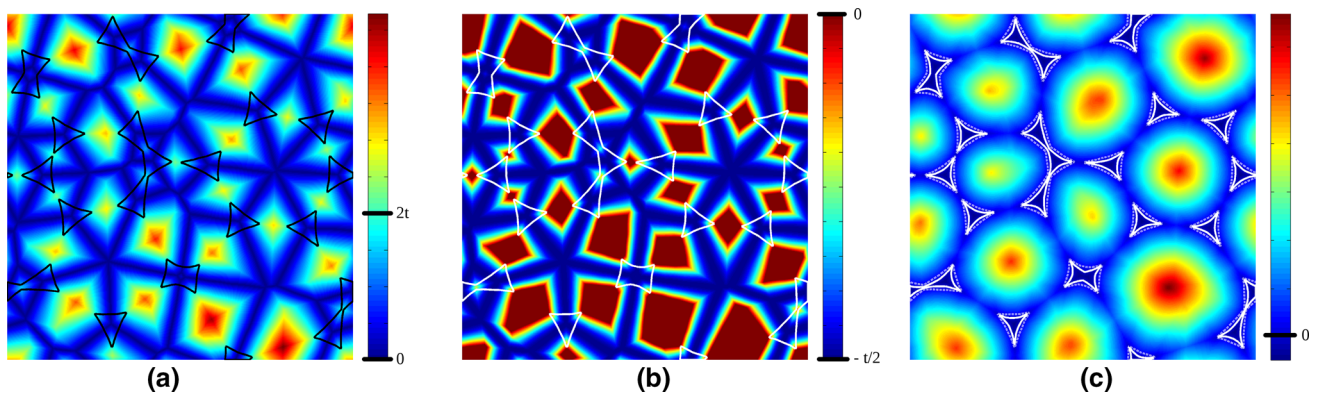


**Fig. 13** Plateau border concavity control, 2D illustration of used function. **a** Operator  $DS_3(\mathbf{x})-DS_2(\mathbf{x})$ . *Black lines* are the  $t$  level set of  $O_P$ . **b**  $O_K(\mathbf{x})$ . *White lines* are the  $t$  level set of  $O_P$ . **c**  $O_P(\mathbf{x}) - t - k.O_K(\mathbf{x})$  *White*

*lines* are the resulting concave Plateau borders and *dashed lines* are the original ones extracted from  $O_P$  alone. (Color figure online)

starting from the middle of the surface to the sharp edge as illustrated in Fig. 13a. The relation (11) turns this operator into a  $C^2$  function that can be used to control the Plateau border concavity replacing (7) by

$$O_P(\mathbf{x}) - t - k.O_K(\mathbf{x}) = 0, \tag{12}$$

with  $0 < k < 1$  controlling the magnitude of the obtained concavity. For the limit  $k = 1$ , the three surfaces of a Plateau border are tangent to each other at sharp edges. The left-hand side of relation (12) is illustrated in Fig. 13c, while extracted 3D geometries are illustrated in Fig. 14.

*Combinations*

Finally, as the relation (10) quite deteriorates the shape of the Plateau borders and the relation (12) does not offer a control on the pore throat closure, one may want to use both concurrently to obtain a larger range of possibilities including all combinations of Plateau border concavities and pore throat closures, i.e. extracting a geometry that will use the cell wall obtained with (10) and the Plateau borders from (12). This is possible with the level set formalism as the minimum of two level set functions is a level set function that defines a surface which is the boundary of the union of domains enclosed by the two initial level sets. So, if  $LS_1(\mathbf{x})$  and  $LS_2(\mathbf{x})$  are the left-hand terms of (10) and (12),

$$\min(LS_1(\mathbf{x}), LS_2(\mathbf{x})) = 0 \tag{13}$$

achieves the intended combination, potentially using two different  $t$  parameters within  $LS_1$  and  $LS_2$ . Figure 15 illustrates the result of this approach for two different sets of parameters. Those can be compared to real samples presenting this kind of morphology, for example in figures of [53].

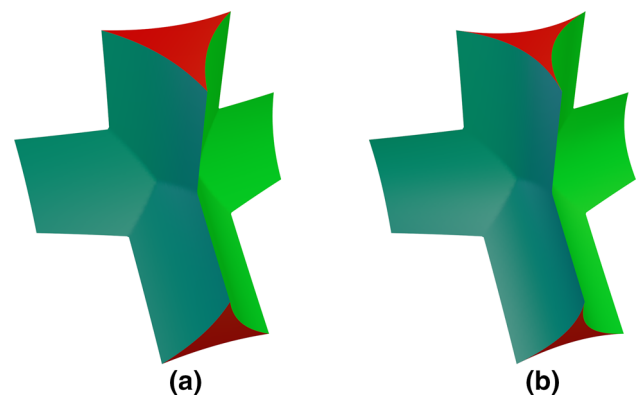


**Fig. 14** Plateau border concavity control, 3D detail. **a**  $k = 0.5$ . **b**  $k = 1$

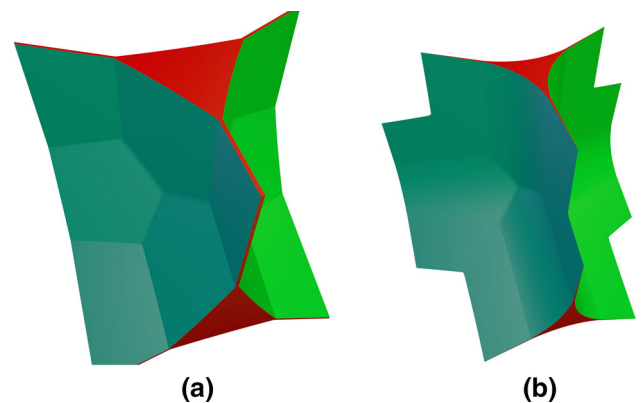


**Fig. 15** Plateau border type combination. **a** Fully closed cell with non-concave Plateau borders. **b** Partially closed cell with concave Plateau borders

**4.2 Spatial variations**

We now show how to introduce some variability in different morphological parameters controlling the generation

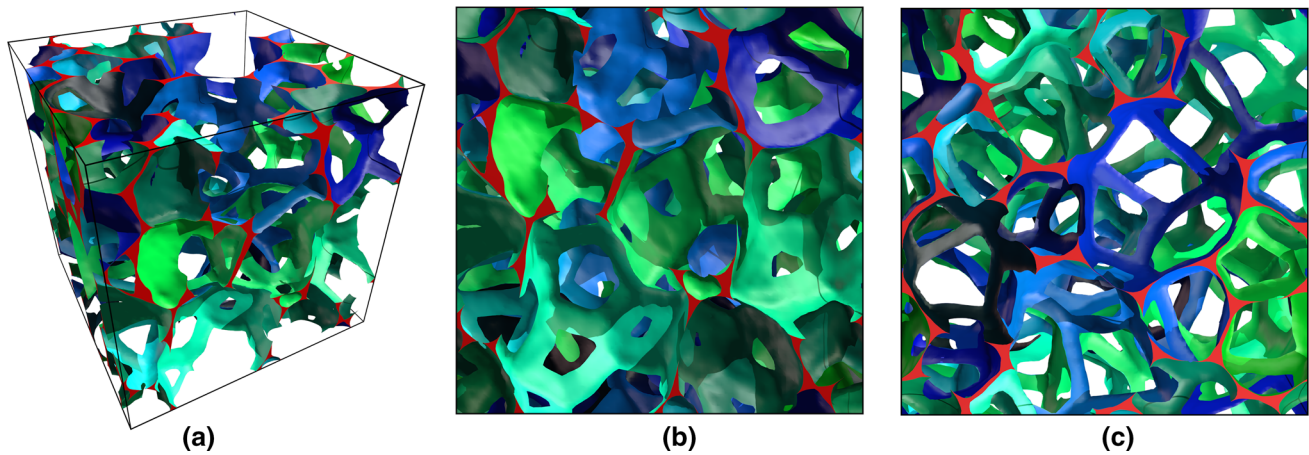


**Fig. 16** Illustration of orientation-sensitive spatial variation for an arbitrary-shaped inclusion base distribution. Wall with *vertical normals* are *fully open* while those with *horizontal normals* are *fully closed*. Other

wall are in an intermediate state. The verticality of closed wall is well visible on the side view. **a** Perspective view. **b** Side view. **c** Top view

process. Several scalar quantities are used to tune the presented level set functions, controlling the wall/strut thickness ( $t$ ), the pore closure rate ( $a$ ), the Plateau borders concavity ( $k$ ) and other parameters that will be further defined. These scalar quantities can also be turned in  $\mathbf{x}$ -dependent 3D functions to control more locally those features.

The simplest thing that can be done to explain the approach is to perform a random variation of the parameters. Here,  $t$  is taken as an example. If a coarse grid  $m^3$  is defined, with  $m \ll n$ ,  $m^3$  random values can be generated, uniformly (or other) distributed between  $t_{\min}$  and  $t_{\max}$  and placed on this grid. Those values can be interpolated (using linear or cubic basis) on the  $n^3$  grid to build a  $T(\mathbf{x})$  field that will be used instead of the constant  $t$  in equations. The spacing  $h_m$  of the  $m^3$  grid determines the “wavelength” of the generated variations. Although this is not specifically illustrated here, the results of this manipulation are visible further in Fig. 21 that serves another purpose.

Since the manipulated distance fields and level set functions inherently include some properties of the geometry, more advanced variations can easily be performed. The example of varying the wall open/closed ratio  $a$  presented in Sect. 4.1 is given here by constructing a global  $A(\mathbf{x})$  field according to the local wall orientation to mimic an anisotropic growth of the foam microstructure. The local orientation of walls is included in the gradient of  $O_V(\mathbf{x})$  and a scalar product of this gradient with a particular direction vector can be used to build the desired  $A(\mathbf{x})$  field. This gradient being hardly discontinuous between two adjacent faces, the resulting  $A(\mathbf{x})$  would better be smoothed before being used. For example, the following formulation will make walls orthogonal to the chosen orientation  $\mathbf{n}$  being open while closing others, those “containing” the orientation  $\mathbf{n}$  presenting the largest thickness:

$$A(\mathbf{x}) = a_{\max} - (a_{\max} - a_{\min}) \cdot \frac{|\mathbf{grad}(O_V(\mathbf{x})) \cdot \mathbf{n}|}{\|\mathbf{grad}(O_V(\mathbf{x}))\|}. \quad (14)$$

The absolute value is added to match only the orientation of  $\mathbf{n}$  and not its direction. The division by the norm of the gradient of  $O_V$  is incorporated to ensure the second term of (14) is between 0 and  $a_{\max} - a_{\min}$ ,  $\mathbf{n}$  being a unit vector. An example of the use of this relation is shown on Fig. 16 for an arbitrary-shaped inclusion base distribution.

### 4.3 Coating phases

We present here a straightforward way to build the geometry of a coating on the generated open foam geometries. A simple distance field-based offset is used here, as already done to extract precipitated or hydration phases on granular geomaterials in [55]. Once the signed distance field of the generated foam  $DS_{\text{FOAM}}(\mathbf{x})$  is known, one can extract the external boundaries of a uniform coating of thickness  $c$  with the level set defined by

$$DS_{\text{FOAM}}(\mathbf{x}) - c = 0. \quad (15)$$

The results of this relation are illustrated on Fig. 17, while  $DS_{\text{FOAM}}$  is illustrated in 2D on Fig. 18a and in 3D in Fig. 20b. The distance field of the foam geometry can either be derived from the level set function it originates from by a distance transform method (e.g. fast marching method [66], vector-transform [67], ...) or by explicitly computing the exact distance from the triangulated geometry. The former is quite light but requires an advanced implementation to reach an acceptable accuracy, while the latter is on the contrary exact

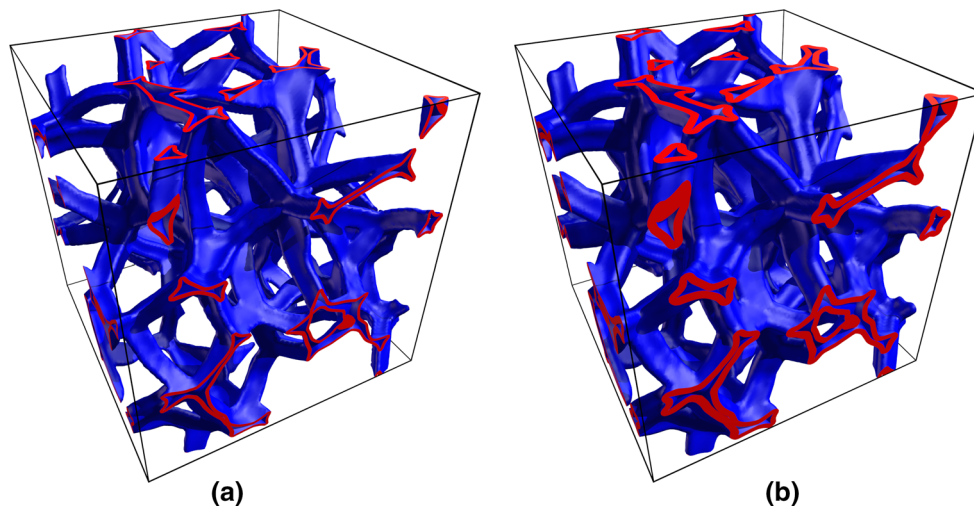


**Fig. 17** Uniform coating forming hollow struts. The underlying foam is generated with  $t = 0.02$ ,  $a = 0$  and  $k = 0.5$ . **a**  $c = 0.01$ . **b**  $c = 0.02$

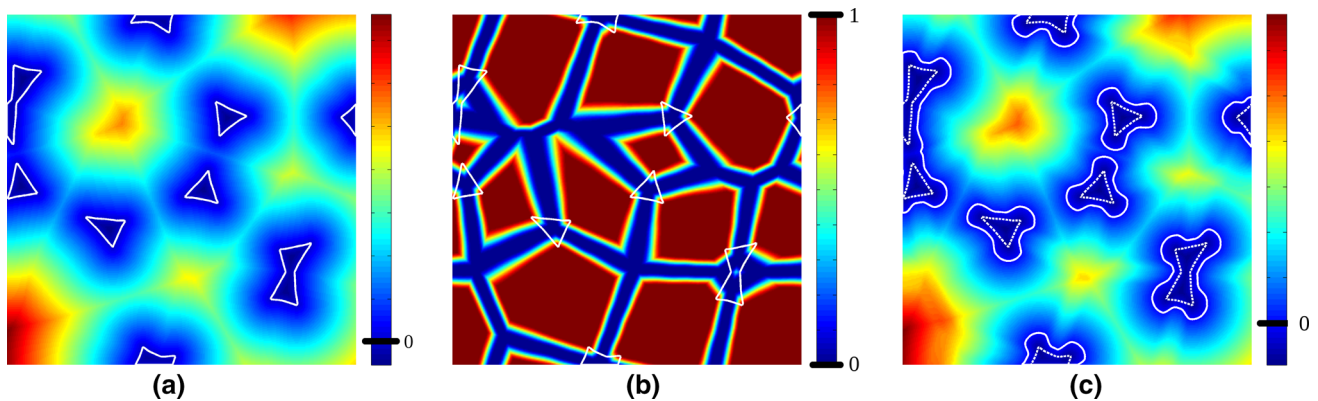


**Fig. 18** Varying thickness coating, 2D illustration of used functions. **a**  $DS_{FOAM}(x)$ . White lines are Plateau border extracted from  $O_P$ . **b** Ramping function  $O_R'(x)$ , with  $r c = 0.2$ . White lines are Plateau border extracted from  $O_P$ . **c**  $DS_{FOAM}(x) - c - d_c . O_R'(x)$ . White plain lines are the extracted coating boundaries. (Color figure online)

but quite computationally intensive. Again, the computation of  $DS_{FOAM}$  may be restricted to a narrow band of interest, more difficult to determine a priori (but it can be done quite approximately using  $O_M$  or  $O_P$  and the norm of their gradient). This can be advantageous with respect to a distance transform approach that generally can stop after a given distance without selecting a priori a domain of interest. However, for the sake of robustness of our experimental implementation, an exact distance computation was used here for this operation.

The excellent quality micrographs and measurements published by Pang et al. in [10] bring the opportunity to add some details to illustrate further the versatility of the proposed approach. The paper by Pang et al. characterized a Ni–Fe foam obtained by coating a sacrificial polymer foam preform and further processed to add a Cr layer on its surface. The material composition of the hollow struts in these foams is heterogeneous; the Ni–Fe precursor exhibits a varying Fe

concentration on the depth of the strut walls, being maximal at mid-depth; the Ni–Fe–Cr foam obtained presents a sharp variation between a Ni–Fe phase (inward) and an Fe–Cr phase (outward). One can also observe in the paper by Pang et al. (especially in Fig. 2b.) that the coating is obviously thicker on sharp edges, probably because of a better adherence of the coating at this particular location.

An increased coating thickness near sharp edges can be obtained by the addition of a term in Eq. (15), subtracting positive values where we want to “push” outward the resulting surface. As for the Plateau border concavity control, the operator  $DN_3(x) - DN_2(x)$  is used as a variable representing the position relative to Plateau border features. In particular, this operator is positive on locus of points closer to a sharp edge than to a border “face”. Then, one could thicken the coating around sharp edges by subtracting a positive value  $d_c$  to the left-hand side of (15) where  $DN_3(x) - DN_2(x)$  is positive. This will give poor results as the thickness of the

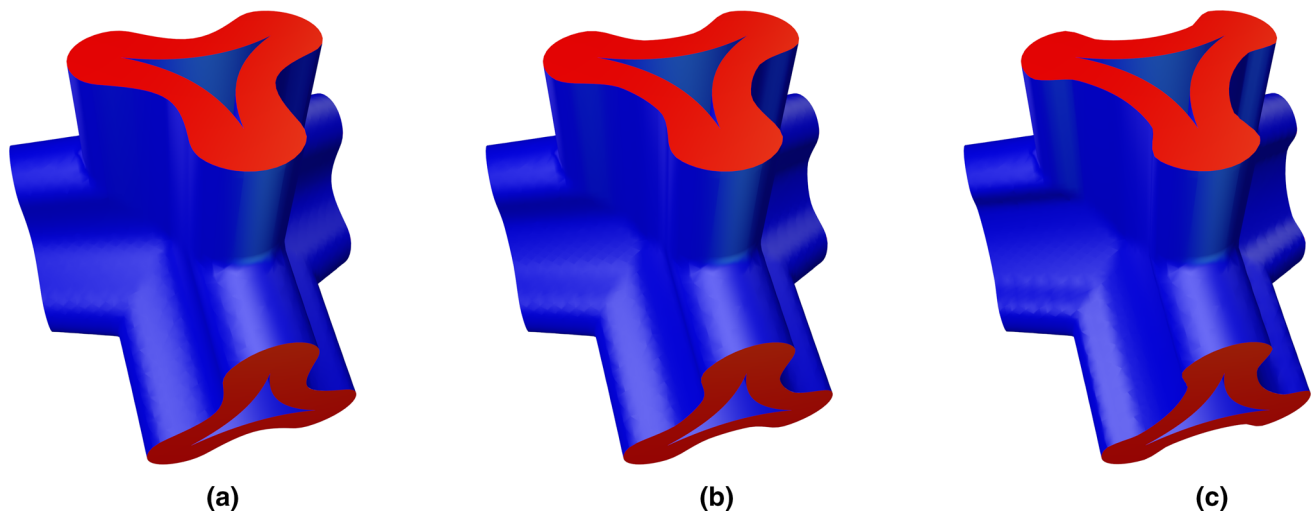


**Fig. 19** Varying thickness coating, 3D Plateau borders detail. The Hermite spline ramping function is used. **a**  $r_c = 0$ . **b**  $r_c = 0.3$ . **c**  $r_c = 0.6$

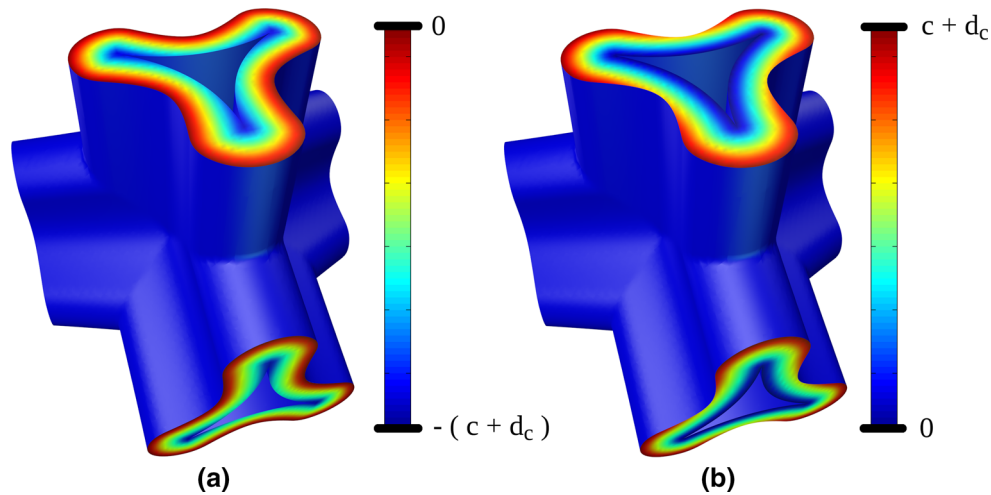


**Fig. 20** Distance functions used for material heterogeneity generation. **a**  $DS_{COAT}(\mathbf{x})$ . **b**  $DS_{FOAM}(\mathbf{x})$

coating will jump sharply from  $c$  to  $c + d_c$ . To fix this, a ramping function is used that will allow a smooth variation of the coating thickness. The linear ramping function used reads

$$O_R(\mathbf{x}) = \max(0, \min(1, ((DN_3(\mathbf{x}) - DN_2(\mathbf{x}))/2 - r_c \cdot t)/(t \cdot (1 - r_c)))) \quad (16)$$

where  $t$  is the same parameter as before and  $r_c$  controls the ramp length. This parameter  $r_c$  should be between 0 and 1, 1 leading to the same result as if the ramping was not applied and 0 producing a ramp that ranges to the middle of the Plateau border faces. As this ramping function is linear, it produces sharp variations of the coating curvature, which may be unwanted. This can be avoided using a cubic Hermite spline interpolation based on  $O_R$  with

$$O'_R(\mathbf{x}) = -2 \cdot O_R(\mathbf{x})^3 + 3 \cdot O_R(\mathbf{x})^2. \quad (17)$$

The varying thickness coating can then be extracted with

$$DS_{FOAM}(\mathbf{x}) - c - d_c \cdot O_R(\mathbf{x}) = 0, \quad (18)$$

using either  $O_R$  or  $O'_R$  as a ramping function. Relation (17) and (18) are illustrated in 2D in Fig. 18b and c, 3D resulting geometry details are shown on Fig. 19.

The potential material heterogeneity of hollow struts can be generated at this stage using the signed distance to the foam  $DS_{FOAM}$  and to the extracted coating  $DS_{COAT}$ . Local relevant values of those functions are illustrated in Fig. 20. Smooth variations, as in the Ni–Fe precursor, can be mapped in a model to a continuous generated function. For sharp variations, as in the Ni–Fe–Cr product, it would be better to extract additional surfaces to represent material interfaces in the model. Such mapping functions and additional sur-

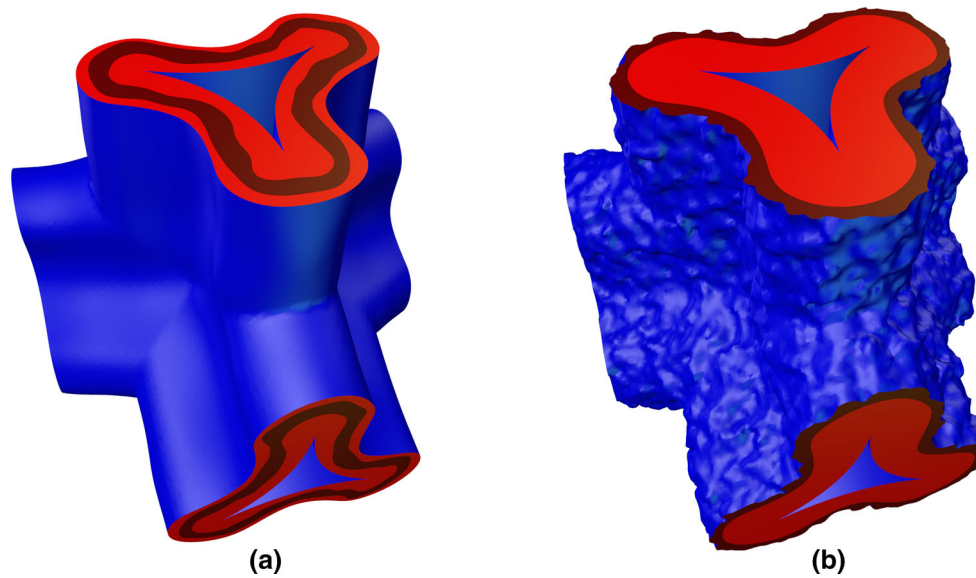


**Fig. 21** Sharp material variation. Additional surfaces are extracted from  $DS_{COAT}$ , random variations are introduced independently for each surface. **a** Three-phase coating. **b** Two-phase coating

faces are built and extracted from  $DS_{FOAM}$  and  $DS_{COAT}$  or a combination of both. Additional variations such as noise and surface roughness can also be added by manipulation of these functions. Some examples of sharp material variations are given in Fig. 21 and can be compared with Figs. 2 and 3 in [10].

## 5 Quantifying morphology of resulting geometries

In order to compare the resulting RVE with real samples, one should be able to quantify some morphological parameters of the obtained geometries. This topic would deserve to be the subject of a specific dedicated work, but we provide here an overview of the ways to evaluate some of the most used parameters.

Some parameters may be evaluated by two main approaches. One “classical” approach makes use of the triangulated surfaces extracted from level set functions by contouring. It requires additional computations and may be harder to implement but will give a very good accuracy even for (reasonably) coarse discretizations. An other “implicit” approach directly makes use of functions already computed during the generation, mainly  $NN_k$ ,  $DN_k$ ,  $O_V$  and  $O_P$ . It requires almost no additional computation but the precision and relevance of the results strongly depend on the discretization size used for those functions.

The first approach makes use of classical algorithms and only essential informations are given here. Some parameters, such as volumes and surfaces can be computed on the final geometry but several others are better computed on the initial tessellation itself. Its geometry can be extracted from

the 0 level set of  $O_V$  but this level set is in practice impossible to extract with a contouring algorithm. Instead, each cell can be extracted separately by contouring the corresponding “inner” version of  $O_V$ . With some additional slicing using operators such as local versions of  $DN_3(\mathbf{x}) - DN_2(\mathbf{x})$  and function  $NN_k$ , isolated tessellation faces, edges and nodes can be also extracted and characterized. Cell volumes, face surfaces, edge lengths, face normal orientations, edge orientations, face-by-cell count, edge-by-face count, dihedral angles and interior angles (we use those two last terms as defined in [52]) can all be computed using this approach. Some of these parameters will not be uniquely defined in the case of arbitrary shaped tessellations (e.g. dihedral angles, face normal orientations, ...), but will be accessible at the level of each related primitive of the contoured geometry. It still remains to properly define the measures of interest in these cases before trying to obtain and use those informations.

In the second approach, parameters such as the number of faces by cell and edges by face can be evaluated directly from function  $NN_k$  as they depend only on the tessellation itself. The number of faces of a cell originating from an inclusion  $i$  is related the number of direct neighbors of this inclusion  $i$  in the original packing. This number is simply the number of distinct value  $NN_2$  takes inside  ${}^1\Theta_i$ . This number can be evaluated for each inclusion in the packing and mean value together with standard deviation can be computed. Similarly, the number of edges of the face separating the inclusions  $i$  and  $j$  is the number of distinct values that  $NN_3$  takes in domains where  $(NN_1(\mathbf{x}) = i) \& (NN_2(\mathbf{x}) = j)$ .

Dihedral and interior angles also depend on the tessellation itself and can be evaluated from  $NN_k$  with the help of  $O_V$ . Let first assume that cell faces are plane and face

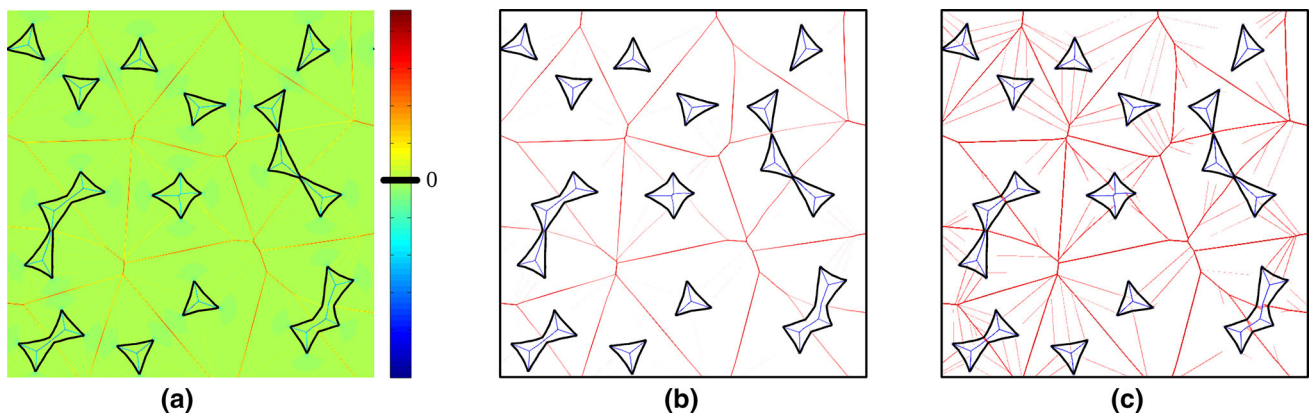


**Fig. 22** Extraction of medial axes, 2D illustration. **a** Sum of the differences on components of the two first order finite difference gradient of  $DS_{FOAM}$ . **b** Medial axes extracted with a high threshold. **c** Medial axes extracted with a low threshold. Spurious branches of medial axis that

would better be discarded are well visible in the “outer” medial axis. On **b** and **c**, blue lines are the “inner” medial axis while red lines are the “outer” one. Indeed, in 3D, medial axes are surfaces. (Color figure online)

edges are straight. The normal to the face separating the cells  $i$  and  $j$  is given by the normalized gradient of  $O_V$  where  $(NN_1(\mathbf{x}) = i) \& (NN_2(\mathbf{x}) = j)$ . This latter is almost constant in this domain if the cell faces are planar. Other faces that share an edge with this face are the common faces of cells  $i$  and  $k$ , with  $k$  taking all values  $NN_3$  takes in the domain where  $(NN_1(\mathbf{x}) = i) \& (NN_2(\mathbf{x}) = j)$ . Dihedral angles at those shared edges can be obtained from the arc-cosine of the scalar product of normals of the two considered faces, while the vector product of those gives a direction vector of the edge. This latter can then be used to compute interior angle with scalar products of director vectors of edges sharing a node. To find these couples of edges, one can use values of  $NN_4$  inside the domain where  $(NN_1(\mathbf{x}) = i) \& (NN_2(\mathbf{x}) = j) \& (NN_3(\mathbf{x}) = k)$ . As  $NN_4$  is not used anywhere else, to avoid computing it for this purpose only (even though it is not expensive), one may also look at values of  $NN_3$  at points adjacent to the domain where  $(NN_1(\mathbf{x}) = i) \& (NN_2(\mathbf{x}) = j) \& (NN_3(\mathbf{x}) = k)$ , considering only points where  $(NN_1(\mathbf{x}) = i) \& (NN_2(\mathbf{x}) = j)$ . It should be mentioned that this procedure can be applied only if cell faces intersect exclusively 3-by-3 and face edges 4-by-4. In the limit of a vanishing discretization size, this should always be the case. However, in practice with finite discretization sizes, situations will arise in which two very close edges (resp. nodes) will be seen as a single one, shared by 4 (resp. 5) or more faces (resp. edges). If a relations graph between cells, faces, edges and nodes is built during the evaluation of angles, such problematic situations can be detected and discarded or taken into account specifically. For arbitrary shaped cells, depending on the quantity of interest, a mean normal for each face can be computed or functions such as  $O_P$ ,  $DS_{FOAM}$  or  $DS_{COAT}$  can be used to select more precisely a domain of interest for computing the gradient of  $O_V$ , for example near edges or in the middle of faces.

In all cases, tessellation cell volumes, the foam volume and the coating phase volume can be evaluated with a reasonable accuracy by counting grid points with relevant values of level set functions, and dividing the obtained number by the total number of grid points. This indeed will give a volume relative to the RVE volume. For the volume of a tessellation cell  $i$ , one should search for points where  $NN_1(\mathbf{x}) = i$ , for the foam volume  $DS_{FOAM}(\mathbf{x}) < 0$  should be used while using  $(DS_{FOAM}(\mathbf{x}) > 0) \& (DS_{COAT}(\mathbf{x}) < 0)$  will allow computing the coating volume.

The medial axis of the resulting foam contains a lot of informations regarding the topology of the microstructure. This medial axis can be extracted by searching for strong discontinuities in the gradient of  $DS_{FOAM}$ . Two medial axes will be extracted, the “inner” medial axis is representative of the wall/strut topology while the “outer” one is related to the void topology. Each component of the gradient of  $DS_{FOAM}$  can be evaluated twice at each grid point by first order finite differences using values at two neighboring grid points. Any difference between those two values for each component reflects a discontinuity of the gradient, the sum of the differences on each component is used as an indicating function to find the medial axis. This function is illustrated in 2D on Fig. 22a. It takes negative values on the “inner” medial axis and positive values on the “outer” one. As the two values of the components of the first order finite difference gradients are always slightly different, a threshold has to be used to extract only “relevant” medial axes. Moreover, the function  $DS_{FOAM}$  is computed as the exact distance to a triangulated mesh for which smooth surfaces are discretized by a patch of plane triangular facets. This introduces spurious medial axes that would not exist for the real smooth geometry. Discontinuity in the gradient due to those spurious medial axes are rather small (or the discretization size is poor with respect to the curvature of the represented geometry) and can also be

discarded with a threshold. This threshold depends on the discretization size and the geometry features and is not trivial to set a priori. It is therefore difficult to give recommendations for its value, but we illustrate its effect by comparing two medial axes obtained with different thresholds on Fig. 22b, c. The value of  $DS_{\text{FOAM}}$  or  $DS_{\text{COAT}}$  on those medial axes can be used to derive average wall/strut thickness and void sizes together with standard deviation. Among these values, one can select only those lying on the tessellation faces (with the help of  $O_V$ ) to isolate the pore throat thickness, or only those lying on the director curve of Plateau border (with the help of  $O_P$ ) to get more precisely the inscribed radius of Plateau borders.

Anisotropy-related parameters such as the fabric tensor [68], the Mean Intercept Length [69] or the Volume Orientation [70] can obviously be computed in the same way as from tomography data, using the level set function from which the final geometry originates, using a criterion  $LS(\mathbf{x}) > 0$  to locate void voxels. In fact, level set functions can be manipulated to create a dummy density map that could be seamlessly imported in usual softwares (e.g. SkyScan) for 3D tomography data analysis to characterize the generated geometries with exactly the same tools as for real scanned samples.

## 6 Discussion

The first point to discuss is the volume discretization of the obtained geometries for their subsequent use in a computational model. Building a good quality finite element mesh may potentially become a major issue when dealing with this kind of RVE in a model. In all cases, the slicing operation used to extract the foam geometry preserving the sharp edges has to be carefully implemented to give a consistent discretization along the sharp edge itself if a classical mesh generator is considered. However, an interesting strategy for building good quality meshes from level set functions was proposed in 2D in [71] and extended to 3D in [72]. By using a dynamic node repositioning using level set functions, this approach is able to mesh very complex geometries with high quality tetrahedral elements. Again, a specific implementation will be required to treat properly the sharp edges as the procedure should be able to use multiple level set functions and to constrain nodes on these sharp edges. If both this approach and classical meshing methods fail to produce usable meshes, one may consider the use of the eXtended Finite Element Method (XFEM) [73, 74]. The XFEM has been developed to use regular non-conforming meshes on complex geometries, by incorporating the geometrical information in a shape function enrichment built from the level set function that implicitly represents it. A particular XFEM setting has also been proposed [75] in order to represent properly

sharp edges with two level set functions and appears particularly well suited for the applications considered here.

Another point we want to discuss here is related to the periodicity of the generated geometries. Periodicity of RVEs may be desired for mainly two reasons. First, enforcing periodic boundary conditions in the generation process is the most satisfying way to discard unwanted boundary effects and achieve statistically homogeneous RVEs. The second reason is related to the homogenization method that is used in a subsequent physical model. Periodic boundary conditions were shown to give the fastest convergence of the homogenized properties while increasing the size of the RVE [76]. The periodicity is enforced in two steps in the generation process, the first is to make the generated foam periodic while the second is required for the coating phase. The only condition for the foam to be periodic is that the functions  $DN_k$  should be periodic, which indeed requires the initial packing to be already periodic. As previously explained in [55], a way to obtain periodic packings together with associated periodic  $DN_k$  functions (which were objectionably denoted “ $LS_k$ ” in that paper) can readily be implemented. It consists in taking into account periodic neighbor copies of each inclusion during the signed distance computation process. In the same paper, a sequential adaptive way to build functions  $DN_k$  in a computationally efficient way was presented. For the generated coating to be periodic, the condition is that the function  $DS_{\text{FOAM}}$  has to be periodic. Just computing the distance to the extracted foam will yield an almost periodic function, but not exactly. When using a distance transform method for the computation of this distance function, a specific implementation should be used in order to propagate the computation front from one side to its periodic counterpart. If an exact Euclidean distance computation is used, parts of the foam geometry located near RVE boundaries (up to a distance relative to the wanted coating thickness) should be duplicated and translated to the opposite side of the RVE. If functions  $DN_k$  are precisely periodic, those duplicated parts will match their periodic relatives exactly and the distance computation will work properly.

Finally, some words should be added concerning the computational efficiency of the method. Indeed, the parameter having the largest influence on the computation time and memory requirements is the size of the evaluation grid  $n^3$ . The RVEs shown in figures of this paper are generally generated with  $n = 60$ , except for some that required a higher resolution and use  $n = 100$  (Figs. 16, 17). The number of inclusions of the initial packing also has an influence on some parts of the process. For instance, a higher number of inclusions in the packing will induce more “local” versions of level set functions to be computed (without requiring storage, see Sect. 3.3). The memory requirement is quite easy to evaluate and is generally not an issue. The major part of the needed storage is used for discretized functions (level

set functions and operators). As a reference, one such function requires 8 Mb in memory for a  $100^3$  grid. Depending on which RVE type is generated and how the generation process is implemented, between 10 and 20 functions of this type would be required, which lead to a rather affordable memory requirement (80 Mb ... 160 Mb for  $n = 100$ ). The number of functions that have to be stored in memory does not depend on the number of inclusions in the initial packing, as each computed  $DS_i$  can be incorporated directly in function  $DN_k$  and can be forgotten before computing the next one. All the useful values of this function are accessible in  $DN_k$  and can be retrieved when required, thanks to function  $NN_k$ . One should then not hesitate to isolate terms of functions in separate variables to clarify the implementation and to ease modifications. Some memory is also required for the extracted geometries, however it is generally small compared to the storage of discretized functions, and strongly depends on the generated geometry. Considering computation times, three main types of operations are performed : vector operations on 3D functions to evaluate level set functions, contouring of 3D functions to extract the geometries and distance field computations. The two first are generally quite light, while, depending on its implementation, the third can have a major influence on the computation time. If a distance transform method is used, this process can remain cheap. It however requires having a level set representation of the inclusions in the initial packing, which may not be the case depending on the inclusion shape generation method. One should also keep in mind that such methods may be inaccurate, even slightly, and could lead to some issues. As a counterpart, exact Euclidean distance evaluation methods can be used but are expensive in 3D. Such a method was used in the present implementation and appeared to be the determinant operation limiting the size of grids used. However, these computations are part of the initialization steps and do not have to be redone for every geometries. For example, for a given initial inclusion packing, once all  $DS_i$  have been computed and stored in  $DN_k$ , all variations of foam morphologies can be performed without doing anything else than vector operations on 3D functions and contouring. Both are quite fast for the grid size used and permit a quasi real-time work. It is worth to recall that if the inclusion packing generation method presented in [55] is used, the function  $DN_k$  are evaluated during the generation process. Functions  $DS_{FOAM}$  and  $DS_{COAT}$  are also computed as an initialization process and several generation trials can be done without recomputing them.

## 7 Conclusion

In this paper, a general approach was introduced to generate RVEs for cellular materials using distance and level

set functions. In this methodology, signed distance fields of inclusions of an initial inclusion packing are used to build neighboring distance functions  $DN_k$  which allow building every level set functions used for the generation process. Several ad-hoc level set functions are formulated to obtain different microstructure morphologies.

First, similarly to our early developments in [55], the “Voronoi” level set function  $O_V$  is introduced to build arbitrary-shaped tessellations from the initial inclusion packing. This function alone is used to produce closed-cell foam RVEs and intermediate situations between a cellular material and a corresponding inclusion-based porous material through the inclusion distribution that generates the tessellation. Then the “Plateau” level set function  $O_P$  is introduced and used to extract open-cell foam RVEs with triangular Plateau border sections. A multi level set slicing operation is then described to avoid problem with sharp edges of Plateau borders at the contouring stage.

Then some operators are proposed to modify the level set functions to generate more subtle Plateau borders shapes. First  $O_V$  and  $O_P$  are combined in a weighted averaging procedure to build intermediate situations between fully open and fully closed cell foams. Then a curvature modifier  $O_K$  is formulated to control the curvature of the generated Plateau borders. Finally, a way to combine two (or more) geometries before the contouring stage is shown to extend the range of possible morphologies.

A procedure to introduce a controlled variability on parameters governing the resulting geometries morphology was explained, either randomly or based on local properties such as wall/strut orientations.

Coated foams were also considered. The signed distance to the generated foam  $DS_{FOAM}$  is used to generate a coating phase on a foam. We described a specific operator  $O_R$  used to generate coating phases presenting an over-thickness near sharp edges of Plateau borders. Hollow struts of metal-coated polymer foam can also be generated together with an associated function that can be used to map the material parameters of a model with the distance to the surface to reproduce potential variation in the composition of the coating, as for example, those described in the particular case of Ni–Fe–Cr foams [10].

Future work is still required to further assess the relevance of the generated geometries. In particular, the morphology of numerical samples should be compared with those of real samples with well established quantitative descriptors. We provided for this purpose the basic ideas that can be used to access these parameters with two different approaches. We emphasized that level set functions produced by the generation process can be used as dummy density maps and the geometry they describe can be analyzed by classical softwares for 3D tomography data post-processing. A part of this future work should be dedicated to figure out efficient

ways to impose a priori some morphological properties of the foam directly as an input of the generation process, instead of having to reach them by a trial-and-error approach.

**Acknowledgments** The F.R.S.-FNRS (Belgium), supporting the first author under the Grant FRIA 5.0.011.12.F and providing computational resources through the Grant FRFC 2.4.626.10.F is acknowledged.

### Appendix

The Plateau level set function  $O_P$  used to extract Plateau border geometry is strongly gradient-discontinuous across  $\Phi_\Theta$ . This gradient-discontinuity is the origin of the sharp edges of Plateau borders, which is a desired feature to be reproduced in RVEs. Discrete level set functions cannot properly define those sharp edges, nor can contouring algorithms extract them without additional information. However, in 3D, a closed surface containing sharp edges can be defined by two (or more) level set functions, the sharp edges being defined as the intersection curves of the two (or more) smooth surfaces they define. The strategy adopted in this work is to define the global geometry as an assembly of smooth surfaces, one for each bubble of the foam, defined by two level set functions each. The first level set function, denoted the “inner” function, defines a closed and smooth surface containing the final surface of interest, the second, denoted the “outer” function is used to slice this surface so that only the subpart of interest remains. Figure 10 summarized this procedure for an isolated bubble. So, for each inclusion in the packing, local “inner” and “outer” versions of the Plateau level set function are built to extract each bubble separately. There is no dedicated formulation for those functions, instead they are built

from their original definition (6), but using local “inner” and “outer” versions of the  $DN_k$  functions, denoted  ${}^I DN_{ki}$  and  ${}^O DN_{ki}$ . This appendix gives some more details on the construction of those functions.

The simple 2D quasi-regular packing of quasi-circular inclusions depicted on Fig. 23a will be used for this explanation. In this figure, inclusions are rendered with distinct colors for easy identification. Local versions of  $DN_k$  are built for the central inclusion ( $i = 1$ ), filled with red. The gradient-discontinuity locus is represented with gray lines while the Plateau borders extracted from  $O_P$  are drawn in bold black. The Fig. 23b is a zoom on Plateau borders shared by inclusion 1 and 2. This particular inclusion couple will be used for explanations, everything being identical for any couple grouping inclusion 1 with any inclusion  $j$  in  $\{2, 3, 4, 5, 6, 7\}$ . On this zoom, level sets defined by both “inner” and “outer” version of the Plateau level set function are drawn in plain and dashed black lines, respectively. The sub-part of the “inner” level set which is conserved after the slicing by the “outer” level set is bold, as well as sharp edges (points in this 2D illustration). The Fig. 24a–d represent the functions  $DN_1, NN_1, DN_2$  and  $NN_2$  for this example packing,  $NN_k$  representations use the same colors for inclusions as Fig. 23a. As mentioned before, the explanation will focus on a particular inclusion couple  $ij$ , and two domains of interest are defined for that :  $A_{ij}$  is the domain where  $(NN_1 = i) \& (NN_2 = j)$ , while  $B_{ij}$  is, conversely, the domain where  $(NN_1 = j) \& (NN_2 = i)$ . Those two domains are adjacent, separated by a subset of  $\Phi_{\Theta_i}$  and are illustrated on Fig. 24d for  $i = 1$  and  $j = 2$ .

The construction of “inner” and “outer” functions is detailed here for  $DN_2$  only, leading to the logical derivation of relations (8b), (8c), (8f) and (8g), the procedure being similar

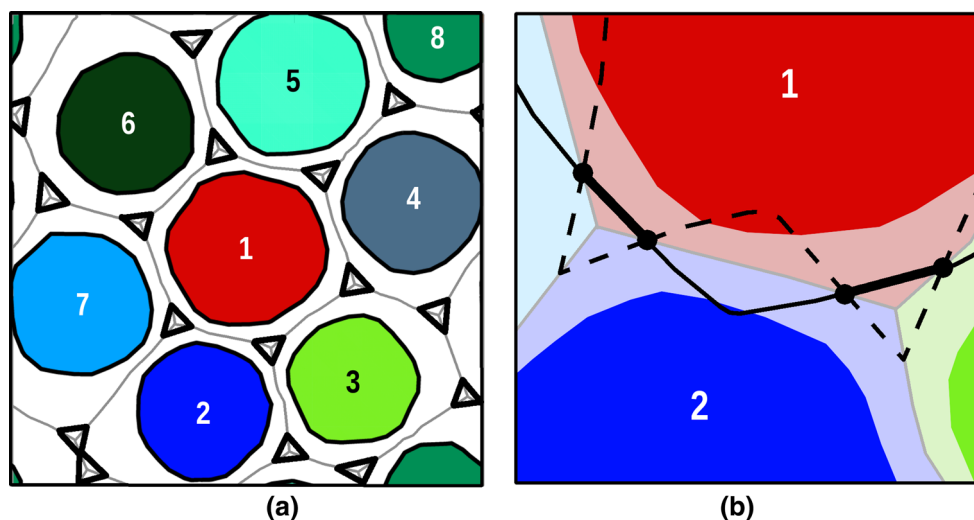


**Fig. 23** 2D example packing. **a** General view. *Grey lines* are  $\Phi_\Theta$  while *bold black lines* are the Plateau borders extracted with  $O_P$ . **b** Zoom on Plateau borders shared by inclusion 1 and 2. The *plain black line* is the

level set of  ${}^I O_{P1}$  while the *dashed line* is the level set of  ${}^O O_{P1}$  used to slice the former. The *bold lines* are the curves remaining after the slicing, *black dots* are the sharp edges. (Color figure online)

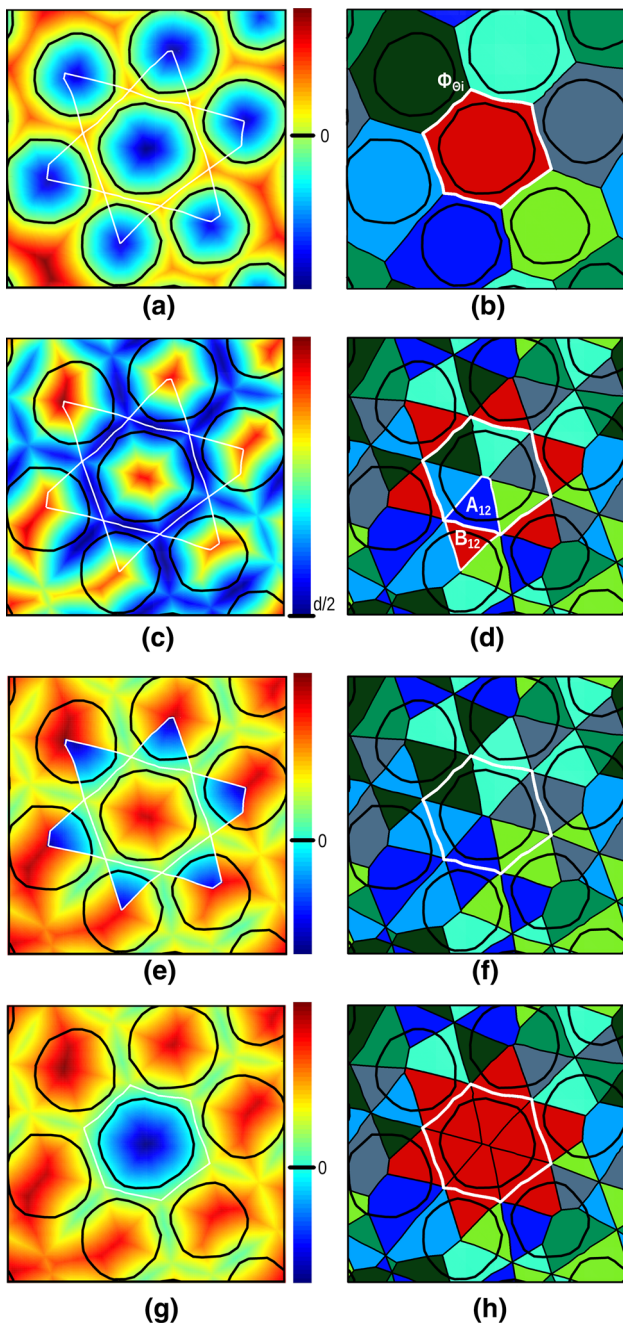


**Fig. 24** 2D illustration of the patch reorganization described by Eqs. (8a)–(8g). **a**  $DN_1(\mathbf{x})$ . **b**  $NN_1(\mathbf{x})$ . The white bold line is  $\Phi_{\Theta_1}$ . **c**  $DN_2(\mathbf{x})$ . The symbol  $d$  denote the distance between the two closer inclusion. **d**  $NN_2(\mathbf{x})$ . Domains  $A_{ij}$  and  $B_{ij}$  are illustrated for  $i = 1$  and  $j = 2$ . **e**  ${}^1DN_{21}(\mathbf{x})$ . **f** Origin of distance values in  ${}^1DN_{21}$ . **g**  ${}^0DN_{21}$ . **h** Origin of distance values in  ${}^0DN_{21}(\mathbf{x})$ . (Color figure online)

and simpler for  $DN_1$ . The origin of the gradient-discontinuity of  $DN_2$  across  $\Phi_{\Theta_1}$  is the change of the second-nearest inclusion across this locus (e.g. successively inclusion 2 then inclusion 1 when going from an arbitrary point in  $A_{12}$  to another in  $B_{12}$ ). Graphically, it can be seen simply by noting that colors on Fig. 24d depicting  $NN_2$  are not the same in

domain  $A_{1j}$  and  $B_{1j}$ , thus values of  $DN_2$  on those domains are not determined from the same inclusion distance field, hence the gradient-discontinuity.

The function  ${}^1DN_{21}$  should be equal to  $DN_2$  inside  ${}^1\Theta_1$  and  $C^1$  continuous across  $\Phi_{\Theta_1}$ , which means that starting from  $DN_2$ , values of  $B_{1j}$  domains should be replaced by the distance field of the inclusion which is  $NN_2$  in the corresponding  $A_{1j}$  domain (inclusion 2 in the illustrated example). The definition of domains  $A_{ij}$  and  $B_{ij}$  implies that the inclusion which is  $NN_2$  in  $A_{ij}$  is  $NN_1$  in  $B_{ij}$ , so values of  $DN_2$  in domains  $B_{ij}$  can be replaced by values of  $DN_1$  to yield  ${}^1DN_{21}$ . As, the union of all  $B_{1j}$  is the domain where  $NN_2 = 1$ , this transformation can be written as

$${}^1DN_{21}(\mathbf{x}) = DN_1(\mathbf{x}) \text{ where } NN_2(\mathbf{x}) = 1. \tag{19}$$

This can be generalized for any inclusion  $i$  to yield Eq. (8c) and completed with Eq. (8b) to represent the conservation of  $DN_2$  values anywhere outside  $B_{ij}$  domains. The resulting  ${}^1DN_{21}$  function is depicted on Fig. 24e, while the origin of distance values is represented on Fig. 24f with the same convention than for  $NN_k$  functions on Figs. 24b and d. It can be seen on this figure that associated  $A_{1j}$  and  $B_{1j}$  domains are now filled with the same color, which means that their values are determined from the distance field of the same inclusions, which ensures the gradient-continuity.

The function  ${}^0DN_{21}$  should be equal to  $DN_2$  on  $\Phi_{\Theta_1}$  and  $C^1$  continuous across it. However, a minimal transformation starting from  $DN_2$  and fulfilling those conditions will also leave the entire  ${}^0\Theta_1$  domains unchanged, altering only values in  ${}^1\Theta_1$  in order to restore the gradient-continuity across  $\Phi_{\Theta_1}$ . The strategy is the opposite to that used for  ${}^1DN_{21}$  and consists in altering the  $A_{1j}$  domains in order to fill it with the distance fields of the same inclusions than distance values in corresponding  $B_{1j}$  domains. By definition of  $B_{ij}$  domains, the inclusion  $i$  is  $NN_2$  in those domains and  $NN_1$  in  $A_{ij}$  domains, values of the latter can then be replaced by values of  $DN_1$  to achieve the intended transformation. As the union of all  $A_{1j}$  domains is the domain where  $NN_1 = 1$ , starting from  $DN_2$ , this transformation can be written as

$${}^0DN_{21}(\mathbf{x}) = DN_1(\mathbf{x}) \text{ where } NN_1(\mathbf{x}) = 1, \tag{20}$$

which can again be generalized for any inclusion  $i$  to yield Eq. (8g) and completed by Eq. (8f) to conserve  $DN_2$  anywhere  $NN_1 \neq i$ . The resulting  ${}^0DN_{21}$  function is depicted on Fig. 24g, while the origin of distance values is represented on Fig. 24h with the same convention than for  $NN_k$  functions. It can be seen on this figure that associated  $A_{1j}$  and  $B_{1j}$  domains are now filled with the same color, which means that their values are determined from the distance field of the same inclusions, which ensures the gradient-continuity.

## References

1. Plateau J (1873) *Statique expérimentale et théorique des liquides soumis aux seules forces moléculaires*. Gauthier-Villars, Paris
2. Taylor JE (1976) The structure of singularities in soap-bubble-like and soap-film-like minimal surfaces. *Ann Math* 103(3):489–539
3. Hollister SJ, Fyhrie DP, Jepsen KJ, Goldstein SA (1991) Application of homogenization theory to the study of trabecular bone mechanics. *J Biomech* 24(9):825–839
4. Qing H, Mishnaevsky L Jr (2009) 3D hierarchical computational model of wood as a cellular material with fibril reinforced, heterogeneous multiple layers. *Mech Mater* 41:1034–1049
5. Song H-W, He Q-J, Xie J-J, Tobota A (2008) Fracture mechanisms and size effects of brittle metallic foams: in situ compression tests inside SEM. *Compos Sci Technol* 68:2441–2450
6. Abbasian Z, Moghbeli MR (2010) Open porous emulsion-templated monoliths: effects of the emulsion preparation conditions on the foam microstructure and properties. *J Appl Polym Sci* 116:986–994
7. Doutres O, Atalla N, Dong K (2011) Effect of the microstructure closed pore content on the acoustic behavior of polyurethane foams. *J Appl Phys* 110:064901
8. Zhang C, Li J, Hu Z, Zhu F, Huang Y (2012) Correlation between the acoustic and porous cell morphology of polyurethane foam: effect of interconnected porosity. *Mater Des* 41:319–325
9. Wichianrat E, Boonyongmaneerat Y, Asavavisithchai S (2012) Microstructural examination and mechanical properties of replicated aluminium composite foams. *Trans Nonferr Met Soc China* 22:1674–1679
10. Pang Q, Wu GH, Xiu ZY, Chen GQ, Sun DL (2012) Synthesis and mechanical properties of open-cell Ni–Fe–Cr foams. *Mater Sci Eng A* 534:699–706
11. Schuler P, Fischer SF, Buhrig-Polaczek A, Fleck C (2013) Deformation and failure behaviour of open cell Al foams under quasistatic and impact loading. *Mater Sci Eng A* 587:250–261
12. Beugre D, Calvo S, Dethier G, Crine M, Toye D (2010) Lattice Boltzmann 3D flow simulations on a metallic foam. *J Comput Appl Math* 234:2128–2134
13. Gerbaux O, Buyens F, Mourzenko VV, Momponteil A, Vabre A, Thovert J-F, Adler PM (2010) Transport properties of real metallic foams. *J Colloid Interface Sci* 342:155–165
14. Burteau A, N'Guyen F, Bartout JD, Forest S, Bienvenu Y, Saberi S, Naumann D (2012) Impact of material processing and deformation on cell morphology and mechanical behavior of polyurethane and nickel foam. *Int J Solids Struct* 49:2714–2732
15. Miedzinska D, Niezgodza T, Gieleta R (2012) Numerical and experimental aluminum foam microstructure testing with the use of computed tomography. *Comput Mater Sci* 64:90–95
16. Roberts AP, Garboczi EJ (2001) Elastic moduli of model random three-dimensional closed-cell cellular solids. *Acta Mater* 49:189–197
17. Meguid SA, Cheon SS, El-Abbasi N (2002) FE modelling of deformation localization in metallic foams. *Finite Elem Anal Des* 38:631–643
18. Czekanski A, Attia MS, Meguid SA, Elbestawi MA (2005) On the use of a new cell to model geometric asymmetry of metallic foams. *Finite Elem Anal Des* 41:1327–1340
19. Kou DP, Li JR, Yu JL, Cheng HF (2008) Mechanical behavior of open-cell metallic foams with dual-size cellular structure. *Scr Mater* 59:483–486
20. Kaoua S-A, Dahmoun D, Belhadj A-E, Azzaz M (2009) Finite element simulation of mechanical behaviour of nickel-based metallic foam structures. *J Alloys Compd* 471:147–152
21. Nammi SK, Myler P, Edwards G (2010) Finite element analysis of closed-cell aluminium foam under quasi-static loading. *Mater Des* 31:712–722
22. Boeckx L, Brennan M, Verniers K, Vandenbroeck J (2010) A numerical scheme for investigating the influence of the three-dimensional geometrical features of porous polymeric foam on its sound absorbing behavior. *Acta Acust United Acust* 96:239–246
23. Sha J, Yip TH, Teo MH (2011) FEM modelling of single-core sandwich and 2-core multilayer beams containing foam aluminium core and metallic face sheets under monolithic bending. *Progr Nat Sci Mater Int* 21:127–138
24. Mangipudi KR, Onck PR (2011) Multiscale modelling of damage and failure in two-dimensional metallic foams. *J Mech Phys Solids* 59:1437–1461
25. Hohe J, Hardenacke V (2012) Analysis of uncertainty effects due to microstructural disorder in cellular or porous materials. *Int J Solids Struct* 49:1009–1021
26. An Y, Wen C, Hodgson PD, Yang C (2012) Investigation of cell shape effect on the mechanical behaviour of open-cell metal foam. *Comput Mater Sci* 55:1–9
27. Perrot C, Chevillott F, Hoang MT, Bonnet G, Becot F-X, Gautron L, Duval A (2012) Microstructure, transport, and acoustic properties of open-cell foams samples: experimental and three-dimensional numerical simulations. *J Appl Phys* 111:014911
28. Hoang MT, Perrot C (2012) Solid films and transports in cellular foams. *J Appl Phys* 112:054911
29. Hosseini SMH, Kharaghani A, Kirsch C, Gabbert U (2012) Numerical simulation of Lamb wave propagation in metallic foam sandwich structures: a parametric study. *Compos Struct* 97:387–400
30. Beckmann C, Hohe J (2012) Assessment of material uncertainties in solid foams based on local homogenization procedures. *Int J Solids Struct* 49:2807–2822
31. El Ghezal MI, Maalej Y, Doghri I (2013) Micromechanical models for porous and cellular materials in linear elasticity and viscoelasticity. *Comput Mater Sci* 70:51–70
32. Hoang MT, Perrot C (2013) Identifying local characteristic lengths governing sound wave properties in solid foams. *J Appl Phys* 113:084905
33. Sir Thomson W (1887) On the division of space with minimum partition area. *Acta Math* 11:121–134
34. Weaire D, Phelan R (1994) A counter-example to Kelvin's conjecture on minimal surfaces. *Philos Mag Lett* 69(2):107–110
35. Raj SV (2011) Microstructural characterization of metal foams: an examination of the applicability of the theoretical models for modeling foam. *Mater Sci Eng A* 528:5289–5295
36. Redenbach C, Shklyar I, Andra H (2012) Laguerre tessellation for elastic stiffness simulations of closed foams with strongly varying cell sizes. *Int J Eng Sci* 50:70–78
37. Fritzen F, Bohlke T, Schnack E (2009) Periodic three-dimensional mesh generation for crystalline aggregates based on Voronoi tessellations. *Comput Mech* 43:701–713
38. Quey R, Dawson PR, Barbe F (2011) Large-scale 3D random polycrystals for finite element method: generation, meshing and remeshing. *Comput Methods Appl Mech Eng* 200:1729–1745
39. Benedetti I, Aliabadi MH (2013) A three-dimensional grain boundary formulation for microstructural modeling of polycrystalline materials. *Comput Mater Sci* 67:249–260
40. Zhang P, Karimpour M, Balint D, Lin J, Farrugia D (2012) A controlled Poisson Voronoi tessellation for grain and cohesive boundary generation applied to crystal plasticity analysis. *Comput Mater Sci* 64:84–89
41. Robert C, Saintier N, Palin-Luc T, Morel F (2012) Micro-mechanical modelling of high cycle fatigue behaviour of metals under multiaxial loads. *Mech Mater* 55:112–129

42. Dahlberg CFO, Faleskog J (2014) Strain-gradient plasticity analysis of the influence of grain size and distribution on the yield strength in polycrystals. *Eur J Mech A/Solids* 44:1–16
43. Massart TJ, Selvadurai APS (2012) Stress-induced permeability evolution in a quasi-brittle geomaterial. *J Geophys Res* 117:B07207
44. Asahina D, Bolander JE (2011) Voronoi-based discretizations for fracture analysis of particulate materials. *Powder Technol* 213:92–99
45. Wei YJ, Anand L (2004) Grain-boundary sliding and separation in polycrystalline metals: application to nanocrystalline fcc metals. *J Mech Phys Solids* 52:2587–2616
46. Sankaran S, Zabarar N (2007) Computing property variability of polycrystals induced by grain size and orientation uncertainties. *Acta Mater* 55:2279–2290
47. Abrivard G, Busso EP, Cailletaud C, Forest S (2007) Modeling of deformation of FCC polycrystalline aggregates using a dislocation-based crystal plasticity model. *AIP Conf Proc* 908:661–666
48. Fan Z, Wu Y, Zhao X, Lu Y (2004) Simulation of polycrystalline structure with Voronoi diagram in Laguerre geometry based on random closed packing of spheres. *Comput Mater Sci* 29:301–308
49. Saxl I, Ponizil P (2001) Grain size estimation: w-s diagram. *Mater Charact* 46:113–118
50. Redenbach C (2009) Microstructure models for cellular materials. *Comput Mater Sci* 44:1397–1407
51. Wejrzanowski T, Skibinski J, Szumbariski J, Kurzydowski KJ (2013) Structure of foams modeled by Laguerre–Voronoi tessellations. *Comput Mater Sci* 67:216–221
52. Vecchio I, Redenbach C, Schladitz K (2014) Angle in Laguerre tessellation models for solid foams. *Comput Mater Sci* 83:171–184
53. Yang C, Zhuang Z-H, Yang Z-G (2014) Pulverized polyurethane foam particles reinforced rigid polyurethane foam and phenolic foam. *J Appl Polym Sci* 131(1):39734
54. Abbasian Z, Moghbeli MR (2011) Preparation of highly open porous styrene/acrylonitrile and styrene/acrylonitrile/organoclay polymerized high internal phase emulsion (PolyHIPE) foams via emulsion templating. *J Appl Polym Sci* 119:3728–3738
55. Sonon B, François B, Massart TJ (2012) A unified level set based methodology for fast generation of complex microstructural multi-phase RVEs. *Comput Methods Appl Mech Eng* 223–224:103–122
56. Lorensen WE, Cline HE (1987) Marching cubes: a high resolution 3D surface construction algorithm. *Comput Graph* 21(4):163–169
57. Cline HE, Lorensen WE, Ludke S (1988) Two algorithms for the three-dimensional reconstruction of tomograms. *Med Phys* 15(3):320–327
58. Ju T, Losasso F, Warren S (2002) Dual contouring of Hermite data. *ACM Trans Graph* 21(3):339–346
59. Nielson GM (2008) Dual marching tetrahedra: contouring in the tetrahedral environment, *Lecture Notes in Computer Science Part I*, 5358 LNCS 183–194
60. Blum H (1967) A transformation for extracting new descriptors of shape. In: *Proceedings Models for Perception of Speech and Visual Form*, pp 362–380
61. Sonon B, Massart TJ (2013) A level-set based representative volume element generator and XFEM simulations for textile and 3D-reinforced composites. *Materials* 6(12):5568–5592
62. Esen Z, Bor S (2011) Characterization of Ti-6Al-4V alloy foams synthesized by space holder technique. *Mater Sci Eng* 528:3200–3209
63. Santa Maria JA, Schultz BF, Ferguson JB, Gupta N, Rohatgi PK (2014) Effect of hollow sphere size and size distribution on the quasi-static and high strain rate compressive properties of Al-A380-Al<sub>2</sub>O<sub>3</sub> syntactic foams. *J Mater Sci* 49:1267–1278
64. Conde Y, Doglione R, Mertensen A (2014) Influence of microstructural heterogeneity on the scaling between flow stress and relative density in microcellular Al-4.5 Cu. *J Mater Sci* 49:2403–2414
65. Huang J, Li Y, Crawfis R, Lu SC, Liou SY (2001) A complete distance field representation. In: *Proceedings of 12th IEEE Visualization*, pp 247–254
66. Sethian JA (1999) *Level set methods and fast marching methods*. Cambridge University Press, New York
67. Satherley R (2001) Vector-city vector distance transform. *Comput Vis Image Underst* 82:238–245
68. Cowin SC (1985) The relationship between the elasticity tensor and the fabric tensor. *Mech Mater* 4(2):137–147
69. Whitehouse WJ (1974) The quantitative morphology of anisotropic trabecular bone. *J Microsc* 101(2):169–176
70. Odgaard A, Jensen EB, Gundersen HJG (1990) Estimation of structural anisotropy based on volume orientation. A new concept. *J Microsc* 157(2):149–162
71. Persson P-O, Strang G (2004) A simple mesh generator in MATLAB. *Soc Ind Appl Math* 46(2):329–345
72. Persson P-O (2005) *Mesh generation for implicit geometries*. Ph.D. Thesis, Massachusetts Institute of Technology, United States
73. Sukumar N, Chopp DL, Moës N, Belytschko T (2001) Modeling holes and inclusions by level sets in the extended finite-element method. *Comput Methods Appl Mech Eng* 190:6183–6200
74. Moës N, Cloirec M, Cartraud P, Remacle J-F (2003) A computational approach to handle complex microstructure geometries. *Comput Methods Appl Mech Eng* 192:3163–3177
75. Moumnassi M, Belouettar S, Béchet E, Bordas SPA, Quoirin D, Potier-Ferry M (2011) Finite element analysis on implicitly defined domains: an accurate representation based on arbitrary parametric surfaces. *Comput Methods Appl Mech Eng* 200:774–796
76. Terada K, Hori M, Kyoya T, Kikuchi N (2000) Simulation of the multi-scale convergence in computational homogenization approaches. *Int J Solids Struct* 37:2285–2311